Single-Chip Silicon Photonic Engine for Analog Optical and Microwave Signals Processing Supplementary Material

Hong Deng, Jing Zhang, Emadreza Soltanian, Xiangfeng Chen, Chao Pang, Nicolas Vaissiere, Delphine Neel, Joan Ramirez,Jean Decobert,Nishant Singh, Guy Torfs, Gunther Roelkens, Wim Bogaerts

1 Monolithic integrated photonic engine

In this supplementary material, we provide more details about our integrated photonic engine for optical and microwave signal process, which is the first single-chip silicon photonics demonstration that can be programmed to perform different analog signal processing functions on both optical and RF signals, and which can function as a black box processor for microwave signals. This chip is fabricated on the imec iSiPP50G silicon photonic platform [1], augmented with transfer-printed III-V semiconductor optical amplifiers (SOA). This makes our processor one of the first demonstrations of transfer-printed lasers integrated in a large circuit on a full silicon photonics platform. Detailed information about the post processing and chip packaging is shown in Supplementary Section 2.

The photonic engine can be programmed to perform many functions, both on optical and electrical signals, which are listed in Supplementary table 1. The photonic engine can combine its tunable laser, modulator, optical filter and photodetector blocks to implement optical signals generation, optical signal modulation, optical signal filtering, and optical signal detection, prospectively. With software control, these optical blocks can be independently characterized, and their functionalities can be demonstrated. Detailed information is shown in Supplementary Section 3.

With all these optical functional elements on chip, the photonic engine can then also perform RF signals generation, RF signal filtering, and RF signal frequency detection with supporting components. No external optical device is needed to operate, calibrate, and control the RF-to-RF functions, which makes the optical internal functions of the photonic engine invisible for the RF signals. This is, to our knowledge, the first microwave photonics processor that functions as a programmable "black box". Conversely, due to the high adaptability of our chip design, this photonic engine can

Single-chip Signal Processor	Optically	Electrically (RF)
Signal Generation	Lasing on-chip	Laser beat Tunable OEO
Signal loading	Reconfigurable Optical Modulation	Reconfigurable Optical Modulation
Signal Filtering (Complex)	Reconfigurable Four Ring-loaded MZI	Reconfigurable RF photonic filters
Signal Detection	Wavelength meter Monitors and RF PD	Frequency measurement

Supplementary Table 1 The functionalities demonstrated with our photonic engine.

seamlessly integrate other off-chip useful devices to enhance its performance. Detailed information on the RF applications of our photonic engine is shown in Supplementary Section 4.

Our chip was built to operate entirely without need for external lab instruments or optical devices. However, because we did not yet integrate RF TIA amplifiers with our photodetectors, we made use of the optical inputs and outputs to insert an external optical amplifier in the optical path for some experiments to overcome the RF crosstalk.

2 Chip Fabrication, Post-processing and Packaging

2.1 Chip Design and Fabrication

The chip is designed with Luceda IPKISS, and fabricated on the imec iSiPP50G silicon photonic platform. This is a standarized silicon photonics platform based on a 220 nm thick silicon-on-insulator (SOI) layer. It supports three waveguide cross sections (strip, rib and deep rib), multiple implantations for high-speed modulators (operating up to 50 GHz in some configurations), germanium photodetectors (PDs), and two layers of Cu damascene metallization. Our chip design and fabrication were based on the standard process flow which is also offered through multi-project wafer services [1, 2].

2.2 Post-processing

The on-chip optical gain is provided by transfer-printed prefabricated semiconductor optical amplifiers (SOAs). III-V SOAs in this work are fabricated based on two epitaxial layer stacks with two multi-quantum wells (MQWs) zone variants to achieve photoluminescence (PL) peaks around 1500 nm and 1550 nm. Using these two epi-stacks in this work leads to laser emissions around 1525 nm and 1575 nm. The micro-transfer-printing (µTP) concept is illustrated in Supplementary Fig. 1.

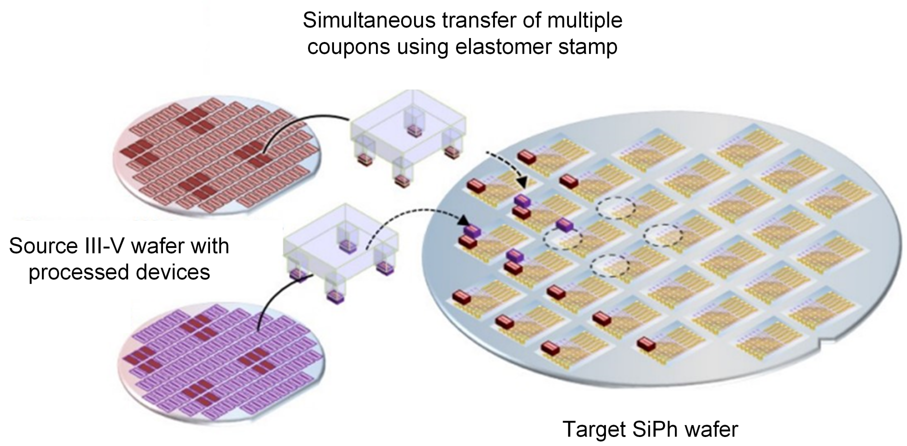

Supplementary Figure 1 The general schematic illustration of µTP concept. SOA coupons from source wafer are transfer-printed on desired locations on the target wafer using PDMS stamp.

Prior to the µTP, a combination of dry-etch (by RIE) and wet-etch (by BHF) was first applied to the photonic chip to locally remove the back-end stack containing 2.5 µm thick silicon dioxide on the Si-waveguide, to form the recess where the InP-based SOA will be integrated. The locally opened recess is slightly longer and wider than the pre-fabricated III-V SOAs. Next, a thin divinylsiloxane bisbenzocyclobutene (DVS-BCB) adhesive layer with a thickness of 150 nm was spray-coated to enhance the bonding strength between the III-V SOA and the underlying Si-waveguide. During the spray-coating, DVS-BCB will build up at the edges of the cavity allowing the metallization in the last step to run over the sidewall of the recess, which here is about 4.5 µm high. µTP of III-V SOAs was done using an X-Celeprint µTP-100 lab-scale printer. The post-printing processing finishes by electrically connecting the printed SOAs to the bondpads of the SiPh back-end using 1 µm thick Au on top of a 40 nm Ti layer. Details for the transfer-printing process are given in [3].

2.3 Chip Packaging

The sample is mounted on a printed circuit board (PCB). The photonic integrated circuit features a total of 15 optical input/output ports, 3 RF ports, 52 thermal tuners, 8 monitor PDs, and at least one transfer-printed laser. As a result, a comprehensive optical, DC, and RF packaging approach is essential to ensure the stability and robustness of the system.

A printed circuit board (PCB) was designed for the electrical connections. The processor chip was placed face-up on the board, and the bondpads were connected to the PCB using wirebonding. A temperature controller is mounted under the PCB, for stabilizing the ambient temperature to 22°Celsius .

The optical packaging process involves the attachment of a fiber array. Specifically, a 32-channel fiber array was positioned with active alignment on the reference waveguide, and then fixed in place with UV-curable glue. The optical transmission spectrum of the reference waveguide was measured with an optical vector analyzer (LUNA, OVA 5000), and the setup is presented in Supplementary Fig. 2(a), with the corresponding transmission plot shown in Supplementary Fig. 2(b). The coupling loss per pair of grating couplers was determined to be 14.7 dB, with the peak transmission at 1543.3 nm.

To encapsulate the electrical bondwires, a significant amount of UV glue was added during the optical packaging process. Unfortunately, this resulted in a somewhat uneven curing process for the fiber array itself, leading to higher-than-normal optical losses. Nevertheless, this measured transmission curve will be used as the normalization reference for all optical responses in Supplementary Section 3.4.

The high-speed PCB consist of a 4-layer stack with high-speed materials (Megtron 6) as dielectric layers. On this board, we mount Rosenberger solderless RF connectors. A straight referencing transmission line (2 cm) shows a 3 dB drop over 40 GHz between two connectors, as shown in Supplementary Fig. 3(a). To evaluate the effect of the bondwires on the RF signal, we wirebonded a pair of transmission lines, and measured the transmission response (half of two transmission line with a bonding wire) as shown in Supplementary Fig. 3(b). The curve in Supplementary Fig. 3(b) is used as reference for the modulator tests (Supplementary Section 3.3). However, because of the different bonding targets, the wirebonding responses for our photonic engine cannot be fully calibrated. On the other hand, we also observe that the PCB introduces RF crosstalk, which couples the RF signal directly from the inputs (of the modulator) to the outputs (of the PD). This measured transmission response is shown in the Supplementary figure 3(c). This curve is later used in the characterization of the on-chip PDs (Supplementary Section 3.5).

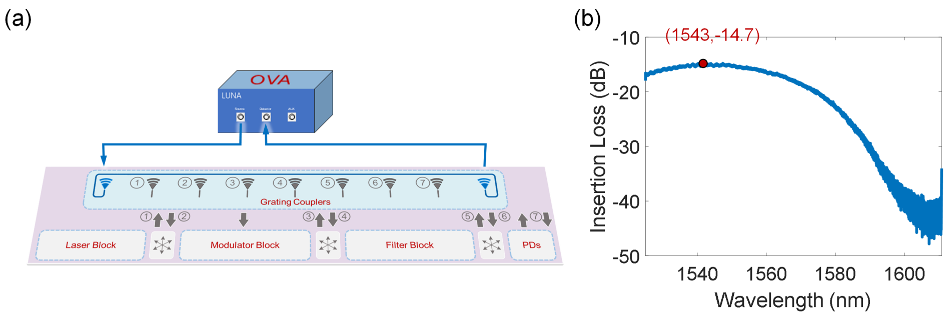

Supplementary Figure 2 (a) The measurement setup for the insertion loss of the reference waveguide. (b) The measured results.

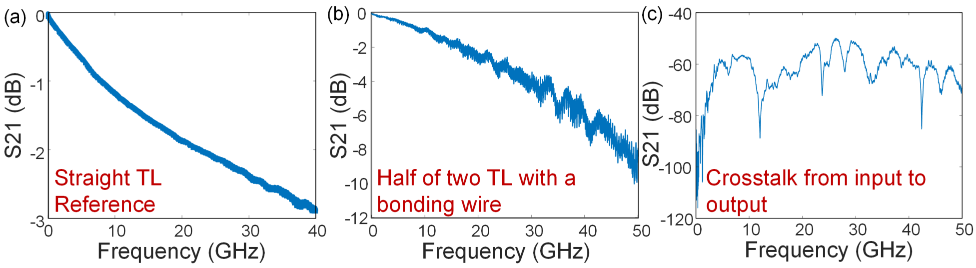

Supplementary Figure 3 (a) Transmission of a reference straight transmission line; (b) Half transmission of two used transmission line with a bonding wire; (c) The direct crosstalk from input RF connector to output RF connector.

3 Characterization of the Individual Functional Blocks

Our single-chip photonic engine contains a laser block, a reconfigurable modulator block, an optical filter block, and two high-speed PDs. Optical switches are placed in between the blocks, allowing us to couple light in or out of the optical path in various points on the chip. This makes it easy for us to measure the response of each individual block. Their characterizations are shown in this section.

3.1 Laser Block: Transfer-Printed Lasers

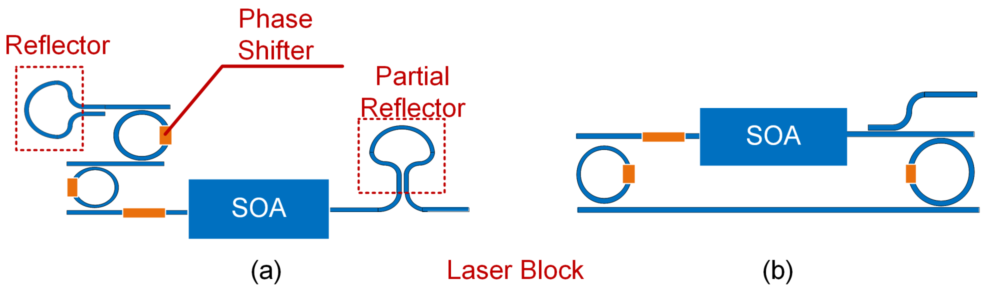

Supplementary Figure 4 Schematic of the laser block. (a) A Fabry–Pérot cavity laser; (b) A ring cavity laser. SOA: Semiconductor optical amplifier.

In our photonic engine, there are two different laser cavities designed in the laser block, which are based on a Fabry–Pérot (FP) cavity and a ring cavity laser, respectively, as shown in Supplementary figure 4. Two ring resonator filters are used in each laser cavity to form a Vernier bandpass filter to select the longitudinal modes. Prefabricated SOA coupons are then transfer printed into the laser cavities to provide optical gain. When the gain from the printed SOA is higher than the other accumulated losses in the laser cavity, lasing will start start in continous-wave (CW) regime. More theoretical analysis and demonstrators of these transfer printed lasers can be found in [3–5].

There are three thermal phase shifters in each laser cavity: two for the phase tuning in the rings and one for the cavity phase. By tuning the phase of the rings and optical cavity, we can tune the lasing wavelength. The laser tuning results are shown in Supplementary figure 5. To be noted is that the FP laser of the packaged sample turned out to be electrically shorted after the wirebonding, so the results shown here were obtained from another sample. The two SOA coupons printed in these two laser cavities come from different III-V source wafers and were designed to have different photoluminescence (PL) peaks around 1500 nm and 1550 nm, leading to lasing peaks around 1525 nm and 1575 nm, respectively. From Supplementary figure 5, both laser cavities can achieve a tunability of more than 50 nm, and the full tuning range of the laser block can reach up to 90 nm.

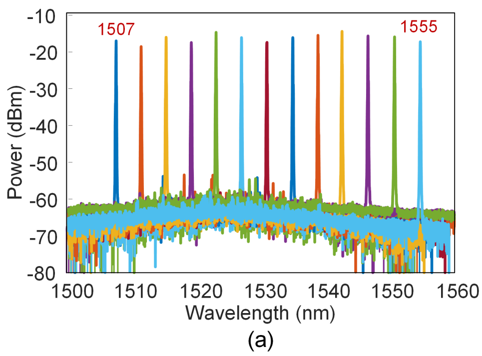

Supplementary Figure 5 Laser tuning results. (a) Using the Fabry–Pérot cavity laser (with another sample); (b)Using the ring cavity laser. The results are measured from grating couplers.

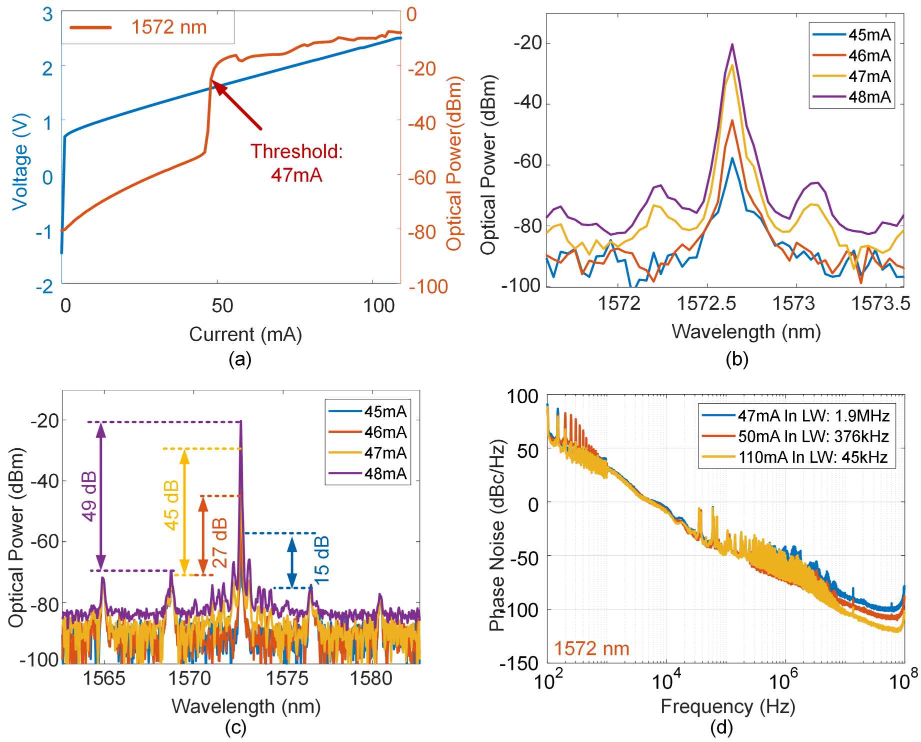

Supplementary Figure 6 (a) Ring laser, voltage v.s. injected current, and optical power v.s. injected current. The lasing threshold is at 47 mA. (b), (c) Optical spectra when the ring laser is pumped by 45 mA, 46 mA (lower than threshold), 47 mA (around threshold), and 48 mA (larger than threshold). (d) Measured lasing phase noises and estimated linewidth with 47 mA, 50 mA, 110 mA injected currents. The optical powers are measured from grating couplers.

These SOAs are energized by injected electrical currents from DC power sources (Keithley 2400). The pumping threshold of the ring laser is illustrated in Supplementary figure 6(a). The ring laser is firstly fine tuned to lase at 1572 nm (highest gain of the printed SOA) with 50 mA injected current. Then, by sweeping the injected current and monitor the output optical power, we can find that the lasing threshold is around 47 mA, corresponding to a current density of 1.836 kA/cm^2. The spectra near the threshold are shown in Supplementary figure 6(b) and (c). Observing these spectra, it is evident that, when the injected current is below 47 mA, the "central" lobe (1572 nm) is not significantly higher than other sidelobes. These sidelobes are presumed to be amplified spontaneous emission (ASE) from the SOA, filtered through the Vernier rings. Beyond the threshold, the central lobe rises rapidly, achieving a side mode suppression ratio (SMSR) of 47 dB with 50 mA injected current. These spectra were measured with an optical spectrum analyzer (Anritsu MS9740A) with a resolution of 30 pm.

Phase noise levels at 1572 nm are assessed by an OEwave OE4000 optical linewidth/phase noise analyzer. Measurements around the threshold (47 mA, 50 mA) and above the threshold (110 mA) yield intrinsic (Lorentzian) linewidths of approximately 1.9 MHz, 376 kHz, and 45 kHz, respectively.

In all subsequent measurements and demonstrations, the lasing wavelength of the ring laser is consistently set to 1552 nm. Supplementary figure 7(a) presents the phase noise of the ring laser at 1550 nm, with an estimated intrinsic linewidth of 143 kHz. A comparison with a commercial laser source (Syntune laser S3600) reveals that our on-chip laser exhibits lower overall phase noise. The stability of the output power is illustrated in Supplementary figure 7(b). Notably, the laser's output power varies by only 0.015 dB over a 600 s timeframe.

3.2 Optical Switches and Tunable Couplers

On-chip 2×2 optical switches are used to connect the functional blocks on the chip and guide light into / out of the optical path. In addition, tunable couplers are used in the

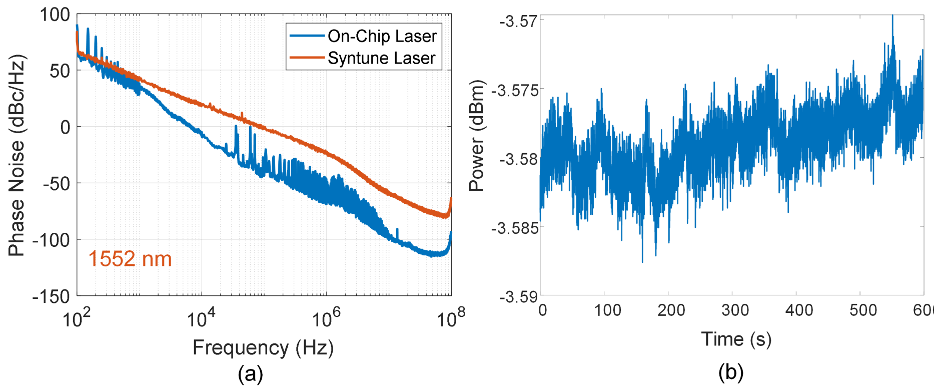

Supplementary Figure 7 (a) Phase noise of the ring laser when lasing at 1552 nm. (b) Stability test of the ring laser.

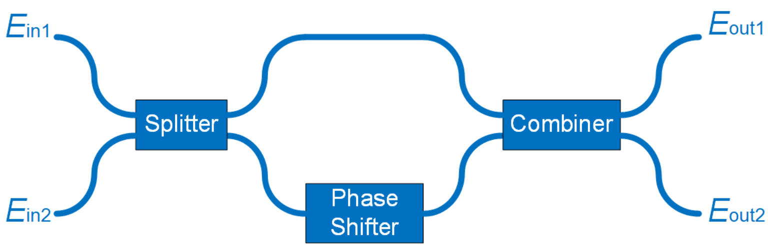

Supplementary Figure 8 A single Mach-Zehnder interferometer.

modulator block and optical filter block to tune the relative power in each path with specific coupling coefficients. In our designs, the optical switches and tunable couplers are achieved by single-stage and double-stage Mach-Zehnder interferometers (MZIs). While a single-stage MZI provides an easy-to-use tunable coupler, it can only cover the full 0-100% coupling range if its splitter and combiner are perfectly balanced. To compensate for possible fabrication imperfections and wavelength dependence, we use a two-stage MZI design, which can provide the full coupler range even with imperfect couplers [6].

We can derive the coupling scheme for the single-stage and two-stage MZI. A schematic for a single-stage MZI is shown in Supplementary figure 8, which includes an optical power splitter, an optical combiner and one phase shifter. The power splitter and the combiner used in our processor are directional couplers (DCs) and the phase shifter is a thermal phase shifter. Then the optical output field can be expressed as:

$$\begin{bmatrix} E_{\text{out1}} \\ E_{\text{out2}} \end{bmatrix} = \begin{bmatrix} \sqrt{(1-\kappa)} & j\sqrt{\kappa} \\ j\sqrt{\kappa} & \sqrt{(1-\kappa)} \end{bmatrix} \begin{bmatrix} 1 & 0 \\ 0 & e^{-j\phi_s} \end{bmatrix} \begin{bmatrix} \sqrt{(1-\kappa)} & j\sqrt{\kappa} \\ j\sqrt{\kappa} & \sqrt{(1-\kappa)} \end{bmatrix} \begin{bmatrix} E_{\text{in1}} \\ E_{\text{in2}} \end{bmatrix} \tag{1}$$

where E_{out1} and E_{out2} are the electrical field at the MZI's outputs, E_{in1} and E_{in2} are the inputs' electrical field, κ is the splitting ratios of the splitter and combiner, and ϕ_s is the phase shift introduced by the phase shifter.

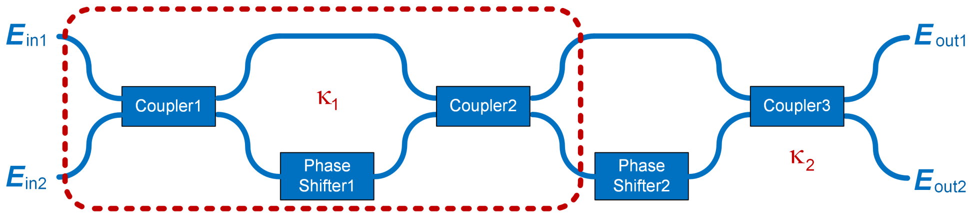

Supplementary Figure 9 A double-stage MZI as a tunable coupler.

If perfect 50:50 DCs are used for the splitter and combiner, the transfer function from E_{in1} to E_{out1} and from E_{in1} to E_{out2} can be expressed as:

$$\boldsymbol{r}_{\text{MZI}} = \frac{E_{\text{out1}}}{E_{\text{in1}}} = \frac{1}{2}[1 - e^{-j\phi_s}] = \sin(\frac{\phi_s}{2})e^{-j\frac{\phi_s}{2}} \tag{2}$$

$$\boldsymbol{\kappa}_{\text{MZI}} = \frac{E_{\text{out2}}}{E_{\text{in1}}} = \frac{1}{2} j[1 + e^{-j\phi_s}] = \cos(\frac{\phi_s}{2}) e^{-j(\frac{\phi_s}{2} - \frac{\pi}{2})} \tag{3}$$

From here we can notice that the output signal's magnitude follows a sinusoidal relation of the half of the ϕ_s , and the output signal's phase is shifted also by half of the ϕ_s. And we can also get the power transformation of the MZI, which is:

$$|\boldsymbol{r}_{\text{MZI}}|^2 = \frac{1 - \cos(\phi_s)}{2} \tag{4}$$

$$|\boldsymbol{\kappa}_{\text{MZI}}|^2 = \frac{1 + \cos(\phi_s)}{2} \tag{5}$$

It can be noted that the power coupling ratios $|\boldsymbol{r}_{\text{MZI}}|^2$ and $|\boldsymbol{\kappa}_{\text{MZI}}|^2$ fully depend on the phase shifts ϕ_s, which makes it an *optical tunable coupler* or *optical switch*[7]. When $\phi_s = 0$, the two arms of the MZI are fully balanced, and all light from input port 1 is coupled to output port 2, which is called the *cross* state, and when the phase difference $\phi_s = \pi$, the light from input 1 is fully coupled to output 1, called the *bar* state.

If the DCs do not have a perfect 50:50 splitting ratio due to the fabrication errors or wavelength dependence, the overall power tuning of the MZI, $|\boldsymbol{r}_{\text{MZI}}|^2$ and $|\boldsymbol{\kappa}_{\text{MZI}}|^2$, cannot be fully tuned of the range of $0 - 1$ with the phase tuning ϕ_s. In that case, a double-staged MZI can be used to release the constraints [6]. With the scheme shown in Supplementary figure 9, the equation 1 can be rewritten as:

$$\begin{bmatrix} E_{\text{out1}} \\ E_{\text{out2}} \end{bmatrix} = \begin{bmatrix} \sqrt{(1-\kappa_2)} & j\sqrt{\kappa_2} \\ j\sqrt{\kappa_2} & \sqrt{(1-\kappa_2)} \end{bmatrix} \begin{bmatrix} 1 & 0 \\ 0 & e^{-j\phi_2} \end{bmatrix} \begin{bmatrix} \sqrt{(1-\kappa_1)} & j\sqrt{\kappa_1} \\ j\sqrt{\kappa_1} & \sqrt{(1-\kappa_1)} \end{bmatrix} \begin{bmatrix} E_{\text{in1}} \\ E_{\text{in2}} \end{bmatrix} \tag{6}$$

where κ_2 is the power coupling ratio of the normal coupler, κ_1 is the power coupling ratio of the tunable coupler, and ϕ_2 is the phase shift from the shifter 2 in Supplementary figure 9. Then the field transfer function can be written as:

$$\boldsymbol{r}_{\text{MZI}} = \sqrt{(1-\kappa_1)(1-\kappa_2)} - \sqrt{\kappa_1\kappa_2} e^{-j\phi_2} \tag{7}$$

$$\boldsymbol{\kappa}_{\text{MZI}} = j\sqrt{(1-\kappa_2)\kappa_1} + j\sqrt{\kappa_2(1-\kappa_1)} e^{-j\phi_2} \tag{8}$$

Then the optical power transfer functions become:

$$|\boldsymbol{r}_{\text{MZI}}|^2 = (1-\kappa_1)(1-\kappa_2) - 2\sqrt{\kappa_1\kappa_2(1-\kappa_1)(1-\kappa_2)}\cos(\phi_2) + \kappa_1\kappa_2 \tag{9}$$

$$|\boldsymbol{\kappa}_{\text{MZI}}|^2 = \kappa_1 + \kappa_2 - 2\kappa_1\kappa_2 + 2\sqrt{\kappa_1\kappa_2(1-\kappa_1)(1-\kappa_2)}\cos(\phi_2) \tag{10}$$

Here we can see that $|\boldsymbol{r}_{\text{MZI}}|^2 + |\boldsymbol{\kappa}_{\text{MZI}}|^2 = 1$. In order to get a full tuning range of coupling ratio [0, 1] for the equation 9 and equation 10, we can set that $|\boldsymbol{r}_{\text{MZI}}|^2 \in [0, 1]$, thus we get:

$$(1-\kappa_1)(1-\kappa_2) - 2\sqrt{\kappa_1\kappa_2(1-\kappa_1)(1-\kappa_2)} + \kappa_1\kappa_2 = 0 \tag{11}$$

$$(1-\kappa_1)(1-\kappa_2) + 2\sqrt{\kappa_1\kappa_2(1-\kappa_1)(1-\kappa_2)} + \kappa_1\kappa_2 = 1 \tag{12}$$

Then from equation 11, we can get:

$$\kappa_1 + \kappa_2 = 1 \tag{13}$$

and from equation 12, we can get:

$$\kappa_1 = \kappa_2 \tag{14}$$

Here, we can know that, if $\kappa_1 + \kappa_2 = 1$, this circuit can be tuned to have a high extinction ratio or closer to 0 at bar state ($|\boldsymbol{r}_{\text{MZI}}|^2 = 0$) and if $\kappa_1 = \kappa_2$, this circuit can be tuned to have a zero loss or closer to 1 at bar state ($|\boldsymbol{r}_{\text{MZI}}|^2 = 1$). In actual fabricated devices, there will be some insertion losses for the DCs and waveguides. This will increase the overall insertion loss of the tunable coupler, and slightly drift the working conditions of κ_1 and κ_2 for compensating loss imbalance.

The first coupler is a tunable coupler discussed above. If we assume that all basic couplers are similar, from equation 10 we can get:

$$\kappa_1 = 2\kappa_2(1-\kappa_2)(1+\cos(\phi_1)) \tag{15}$$

where ϕ_1 is the phase shift from the shifter 1 in Supplementary Fig. 9. Substituting equation 15 into equation 13 and equation 14 we can get:

$$\frac{1}{2\kappa_2} = 1+\cos(\phi_1) \tag{16}$$

$$\frac{1}{2(1-\kappa_2)} = 1+\cos(\phi_1) \tag{17}$$

For a tunable ϕ_1, we can get:

$$\kappa_2 \in [0.25, 0.75] \tag{18}$$

which means that if the power coupling ratio of the fabricated couplers locates in [0.25, 0.75], the full double-stage MZI's power coupling ratio can be tuned from 0 to 1, by tuning the two phase shifters.

We characterized our double-stage MZI responses in our photonic engine. Two phase shifters are electrically driven to tune the ϕ_1 and ϕ_2 , individually, and the results are shown in Supplementary Fig. 10.

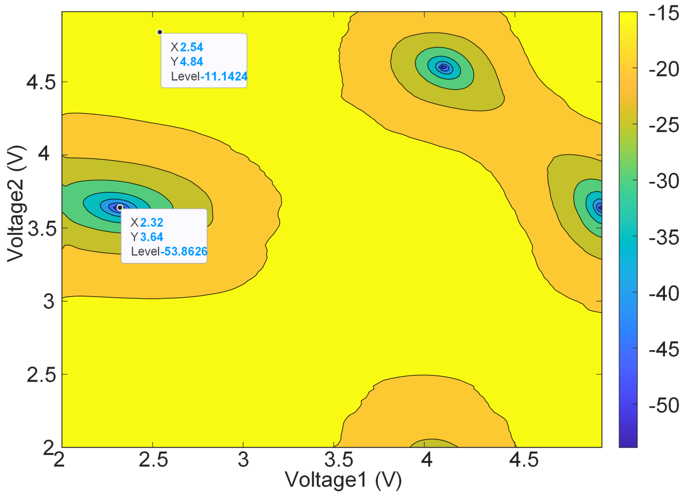

Supplementary Figure 10 Double-stage MZI test results. The contour plot shows the output optical power from port out1.

As can be seen, when tuning the two phase shifter, the output optical power can be tuned from −11 dBm to −53 dBm, reaching a extinction ratio of 42 dB at bar port.

3.3 Modulator Block: Reconfigurable modulator

The reconfigurable modulator is an MZI formed with two tunable couplers, a PN junction based high speed phase modulators, two thermal phase shifters and two tap monitors. The scheme is shown in Supplementary Fig. 11. In this modulator design, a full tuning range for the tunable couplers' κ is preferred, thus we used double-stage MZI structures to form the

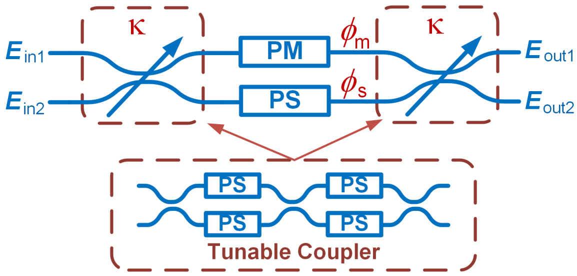

Supplementary Figure 11 Scheme of the modulator block. PM: Phase modulator. PS: Phase shifter. TC: Tunable coupler.

tunable coupler. We operate the modulator block in bar state, i.e. it's optical input and output are on the same side as the arm with the high-speed PN modulator. In this configuration, the modulator's tunable couplers' coupling ratio κ are set to be equal to ensure the lowest insertion loss of the whole modulator block (equation14). Like with the tunable coupler, we can write out the transmission of the modulator subcircuit, and equation1 can be rewritten as:

$$\begin{bmatrix} E_{\text{out1}} \\ E_{\text{out2}} \end{bmatrix} = \begin{bmatrix} \sqrt{(1-\kappa)} & j\sqrt{\kappa} \\ j\sqrt{\kappa} & \sqrt{(1-\kappa)} \end{bmatrix} \begin{bmatrix} \alpha e^{-j\phi_m} & 0 \\ 0 & e^{-j\phi_s} \end{bmatrix} \begin{bmatrix} \sqrt{(1-\kappa)} & j\sqrt{\kappa} \\ j\sqrt{\kappa} & \sqrt{(1-\kappa)} \end{bmatrix} \begin{bmatrix} E_{\text{in1}} \\ E_{\text{in2}} \end{bmatrix} \tag{19}$$

where α is the loss factor of the PN modulator, ϕ_s represents the relevant phase difference of the two arm (tuned by the phase shifter), and ϕ_m is the modulator introduced phase shift, which can be expressed as:

$$\phi_m = \frac{\pi}{V_\pi} V_{\text{rf}} \cos(\omega_{\text{rf}} t + \phi_{\text{rf}}) \tag{20}$$

In which the $V_{\text{rf}}\cos(\omega_{\text{rf}} t + \phi_{\text{rf}})$ is the modulation RF signal.

Here we assume that the loss of the PN modulator is unrelated with the modulation signal to simplify the modulated signal's expression, which means the PN modulator acts as a pure phase modulator. For an actual PN junction-based phase modulator, there will be a slight spurious intensity modulation, which will be discussed later. The derivation holds for actual devices, but all configurations will be slightly different depending on the actual device characteristics.

Assuming the light signal $E_{\text{in1}} = e^{-j(\omega_c t)}$ is fed from input 1, the modulated light signal at bar port can be expressed as:

$$E_{\text{out1}} = [(1-\kappa)\alpha e^{-j\phi_m} - \kappa e^{-j\phi_s}] E_{\text{in1}} \tag{21}$$

Using the Jacobi–Anger expansion,

$$\begin{aligned} e^{-j\phi_m} &= e^{-j[\pi \frac{V_{\text{rf}}}{V_\pi} \cos(\omega_{\text{rf}} t + \phi_{\text{rf}})]} \\ &= \sum_{n=-\infty}^{\infty} i^n J_n(\frac{\pi}{V_\pi} V_{\text{rf}}) e^{-jn(\omega_{\text{rf}} t + \phi_{\text{rf}})} \end{aligned} \tag{22}$$

where J_n is is the n-th Bessel function of the first kind, we can expand equation21 as:

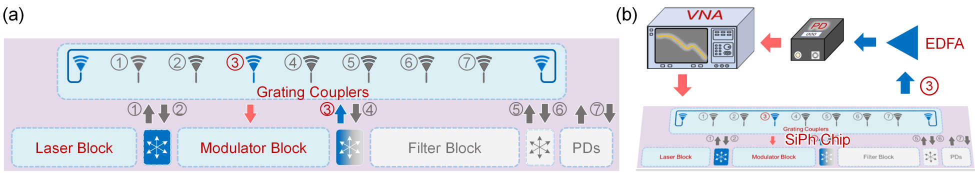

Supplementary Figure 12 (a)Sample configuration to test the modulator block. (b) The setup for the measurement. VNA: Vector Network Analyzer; PD: Photodetector. SiPh sample: Silicon photonic sample. EDFA: Erbium-doped fiber amplifier.

$$
\begin{aligned}
E_{\text{out1}} &= [(1-\kappa)\alpha \sum_{n=-\infty}^{\infty} j^n J_n(\frac{\pi}{V_\pi}V_{\text{rf}})e^{-jn(\omega_{\text{rf}}t+\phi_{\text{rf}})} - \kappa e^{-j\phi_s}]e^{-j(\omega_c t)} \\
&\simeq [(1-\kappa)\alpha J_0(\frac{\pi}{V_\pi}V_{\text{rf}}) - \kappa e^{-j\phi_s}]e^{-j(\omega_c t)} + \\
&j(1-\kappa)\alpha J_1(\frac{\pi}{V_\pi}V_{\text{rf}})(e^{-j((\omega_c-\omega_{\text{rf}})t-\phi_{\text{rf}})} + e^{-j((\omega_c+\omega_{\text{rf}})t)\phi_{\text{rf}}}) \\
&= A_0 e^{-j\phi_{A_0}} e^{-j(\omega_c t)} + jA_1(e^{-j((\omega_c-\omega_{\text{rf}})t-\phi_{\text{rf}})} + e^{-j((\omega_c+\omega_{\text{rf}})t+\phi_{\text{rf}})})
\end{aligned} \tag{23}
$$

Here, only the first sidelobes are kept. The gain of the carrier and left and right modulated sideband are given by

$$
\begin{aligned}
A_0 e^{-j\phi_{A_0}} &= (1-\kappa)\alpha J_0(\frac{\pi}{V_\pi}V_{\text{rf}}) - \kappa e^{-j\phi_s} \\
A_1 &= (1-\kappa)\alpha J_1(\frac{\pi}{V_\pi}V_{\text{rf}})
\end{aligned} \tag{24}
$$

When this modulated light signal is received by a PD, we can get the photocurrent with the square law detection, which can be expressed as:

$$
\begin{aligned}
I_{\text{PD}} &= \mathcal{R}E_{\text{out1}}E^*_{\text{out1}} \\
&= \mathcal{R}[A_0 e^{-j\phi_{A_0}} e^{-j(\omega_c t)} + jA_1(e^{-j((\omega_c-\omega_{\text{rf}})t-\phi_{\text{rf}})} + e^{-j((\omega_c+\omega_{\text{rf}})t+\phi_{\text{rf}})})] \\
&\times [A_0 e^{j\phi_{A_0}} e^{j(\omega_c t)} - jA_1(e^{j((\omega_c-\omega_{\text{rf}})t-\phi_{\text{rf}})} + e^{j((\omega_c+\omega_{\text{rf}})t+\phi_{\text{rf}})})] \\
&= \mathcal{R}(A_0^2 + 2A_1^2 - 4A_0A_1\sin(A_0)\cos(\omega_{\text{rf}}t+\phi_{\text{rf}}) + 2A_1^2\cos(2\omega_{\text{rf}}t + 2\phi_{\text{rf}}))
\end{aligned} \tag{25}
$$

where $\mathcal{R}$ is the responsibility of the used PD.

Then we can know that the field amplitude of the recovered RF signal at the original frequency is (with equation24):

$$
\begin{aligned}
I_{1^{st}} &= -4\mathcal{R}A_0A_1\sin(\phi_{A_0})\cos(\omega_{\text{rf}}t+\phi_{\text{rf}}) \\
&= 4\mathcal{R}\kappa(1-\kappa)\alpha J_1(\frac{\pi}{V_\pi}V_{\text{rf}})\sin(\phi_s)\cos(\omega_{\text{rf}}t+\phi_{\text{rf}})
\end{aligned} \tag{26}
$$

which is determined by the coupling ratio of the tunable couplers κ and the phase shifter's phase change ϕ_s.

The recovered RF signal at the original frequency can also be expressed as:

$$
\begin{aligned}
I_{1^{st}} &= -4\mathcal{R}A_0A_1\sin(\phi_{A_0})\cos(\omega_{\text{rf}}t+\phi_{\text{rf}}) \\
&= -2\mathcal{R}A_0A_1[\sin(\omega_{\text{rf}}t+\phi_{\text{rf}}+\phi_{A_0}) + \sin(-\omega_{\text{rf}}t-\phi_{\text{rf}}+\phi_{A_0})] \\
&= -2\mathcal{R}A_0A_1[\sin(\omega_{\text{rf}}t+\phi_{\text{rf}}+\phi_{A_0}) - \sin(\omega_{\text{rf}}t+\phi_{\text{rf}}-\phi_{A_0})]
\end{aligned} \tag{27}
$$

This signal consists of the two modulated optical sidebands that are downconverted with the optical carrier after the square law detection by the photo diode. The relative phase of

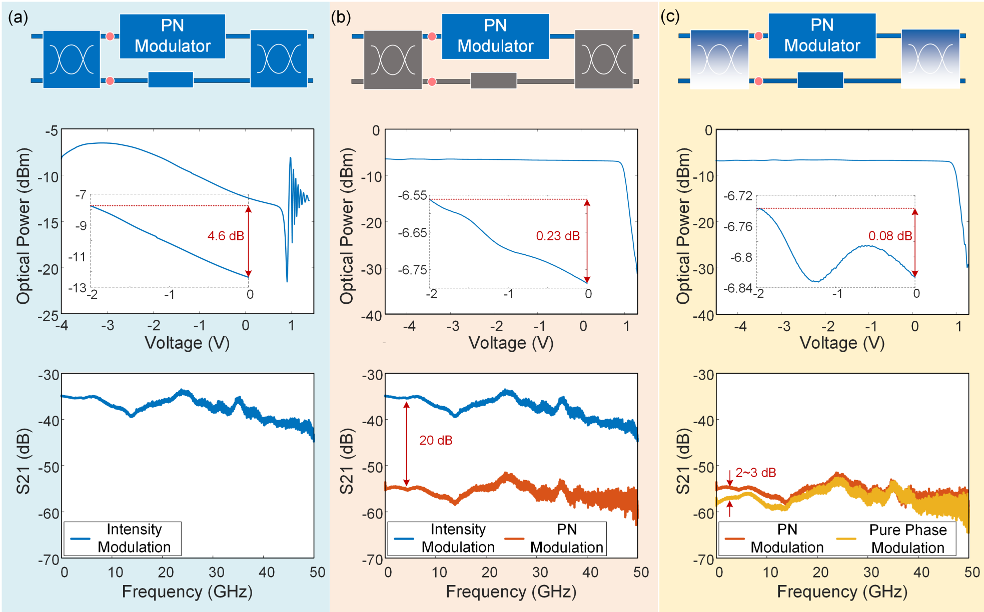

Supplementary Figure 13 (a)A configured intensity modulator and its responses; (b) Only the PN junction modulator used, and its spurious intensity modulated response compared to the modulator configured as intensity modulator; (c) A configured pure phase modulator and its reduced spurious intensity modulation. The first row: the configuration of the modulator block. The second row: DC sweep on the PN junction modulator. The third row: the frequency response of the modulator block.

the two signals ($2\phi_{A_0}$) can be tuned by the phase shifter (ϕ_s), which can be calculated with equation 24.

Indeed, when $\kappa = 0$, all light goes through the PN modulator and ϕ_{A_0} is zero, so no signal will be detected after the photodiode as the light was purely phase modulated, if the PN modulator is treated as an ideal phase modulator.

However, when $\kappa = 0.5$, half of the light goes through the phase modulator and the modulator block is configured as an MZ intensity modulator, which can be verified with equation 26 when $\kappa(1-\kappa)$ and $\sin\phi_s$ are maximized. To enable both working conditions, the full κ tuning range is required, which is why double-stage MZI structures are employed as tunable couplers.

The modulator block is measured with the setup shown in Supplementary Fig. 12. We used the on-chip laser block and the modulator block to load the RF signal generated by a VNA (Keysight E8364B, 50 GHz) onto an light carrier, and the light signal was coupled out of the chip and received by a standalone off-chip PD (Discovery LabBuddy DSC10H, 43 GHz) to be converted back to an RF signal. The VNA received the recovered RF signal and compared it with what it generated, which corresponds to the S21 scatter parameter of the system under test.

The measured S21 results of the modulator block are shown in Supplementary Fig. 13. The modulator block can be configured as an intensity modulator, a regular PN junction modulator, and an optimized pure phase modulator. If the tunable couplers' $\kappa = 0$, the modulator block will be simplified to a PN junction based phase modulator. The DC sweep on the PN junction is shown in the middle of Supplementary Fig. 13(b). As can be seen,

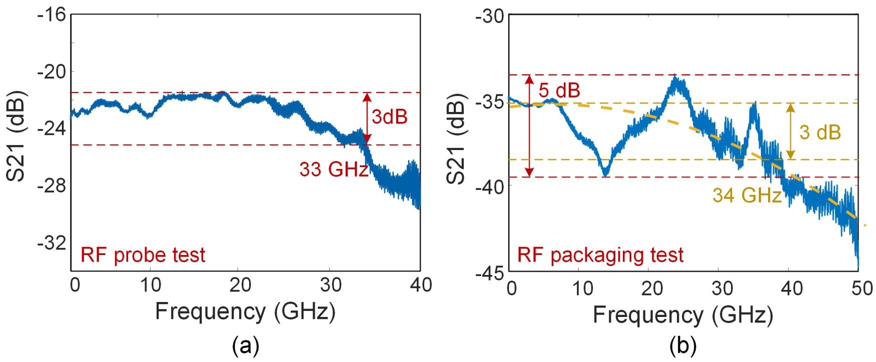

Supplementary Figure 14 Modulator frequency response. (a) Tested with RF probes. (b) Tested with full packaging.

the PN junction has an absorption variance with the applied voltage at its depletion mode, which will introduce spurious intensity modulation. However, by guiding a little bit light to the other arm of the MZI, this spurious intensity modulation can be suppressed [8], and the resulting pure phase modulation response is shown in Supplementary Fig. 13(c). Ideally, if the tunable couplers' κ is set to around 0.5, the modulator block would work as a Mach-Zehnder Modulator for intensity modulation. Due to the modulator arm has a higher insertion loss than the phase shifter arm, the splitter is set to distribute more light into the modulator arm to balance the optical power and get a higher modulation depth. This intensity modulation responses are shown in Supplementary Fig. 13(a). In this measurement, the output power of the Erbium-doped fiber amplifier (EDFA) is fixed at 7.8 dBm and the photo current of the PD is fixed at 3.2 mA.

The modulator blocks in other samples were also measured with RF probes individually, and they showed good uniformity with a 3 dB bandwidth of 33 GHz as intensity modulators, which matched the data in PDK handbook (33.8 GHz biased at -1 V), as shown in Supplementary Fig. 14(a). Compared with the probed modulators, the wirebonding packaged one shows some extra resonance in its response after the calibration, as shown in Supplementary Fig. 13(a) and Supplementary Fig. 14(b). The resonance was limited within 5 dB, while the second-degree polynomial fit still shows a 3 dB bandwidth of 34 GHz. The absolute RF loss difference is due to the optical power difference (10 dBm off-chip laser vs on-chip laser).

3.4 Filter Block: Ring-loaded MZI

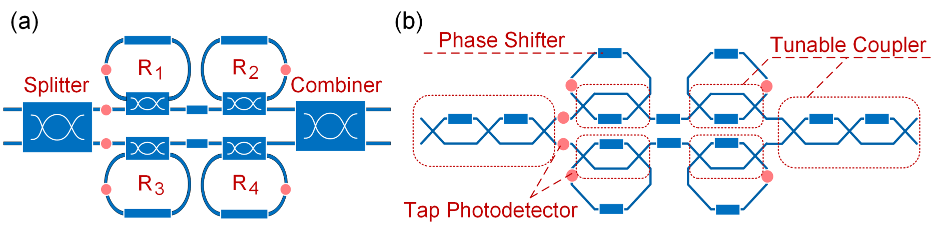

Supplementary Figure 15 Schematic of the filter block: Four ring loaded MZI.

A multistage ring-loaded MZI with tunable couplers can reach arbitrary magnitude responses by tuning all phase and coupling ratios. In our photonic engine, we used a MZI structure with two cascaded rings on both two arms, see in Supplementary Fig. 15. The cascaded rings on each arm work as a second-order all-pass filter (if lossless), and the combiners mix them up (equation 6). Classical bandpass filters can be achieved by the sum or difference of two all-pass filters [9]. If the desired response fluctuates between two levels, the bandpass filter design approach can be used with specific MZI coupling ratios, where maximum and minimum of the main MZI spectrum depends on the coupling ratios of the splitter and the combiner (equation 13 and equation 14). A more generic filter design can be achieved with the characteristic function approach [10].

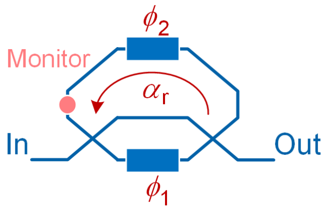

Supplementary Figure 16 A ring resonator with a tunable coupler

A tunable coupler's transmission can be found as equation 2 and equation 3, and the waveguide transmission can be expressed as $\alpha_r e^{-j\phi_2}$ where α_r is the ring's propagation loss factor and the ϕ_2 is the ring's phase shifts. Then, the transfer function of a ring resonator with a tunable coupler, as shown in Supplementary Fig. 16, can be expressed as:

$$\frac{E_{\mathrm{Out}}}{E_{\mathrm{In}}} = \frac{\sin(\phi_1/2)e^{-j(\phi_1/2+\pi/2)} - \alpha_r e^{-j(\phi_1+\phi_2)}}{1+\alpha_r e^{-j(\phi_2)}\sin(\phi_1/2)e^{-j(\phi_1/2+\pi/2)}} \tag{28}$$

Because α_r cannot be one (lossless), the ring resonator will not be a perfect all-pass filter and will have a free spectral range (FSR), which can be calculated as [11]:

$$\mathrm{FSR} = \frac{\lambda^2}{n_g L} \tag{29}$$

where λ is the optical carrier wavelength, n_g is the group index of the waveguide and L is the round trip length of the ring resonator.

The MZI structure in our photonic engine is designed to be balanced, leading to a near-infinite FSR. The ring resonators we used in our photonic engine are designed identically, thus their FSR is very similar, and so this defines the FSR of the entire filter block. By tuning the splitter and the combiner's coupling ratio κ to either 0 or 1, we can measure the transmission of a single ring. The measurement setup is shown in Supplementary Fig. 17(a), and the results are shown in Supplementary Fig. 17(b)-(e). As can be seen, these four rings show an FSR of 0.86 nm or 107.5 GHz. Due to the embedded tunable coupler, the ring's length is relatively large and the FSR is small. A larger FSR can be achieved with a more compact tunable coupler.

The full width at half-maximum (FWHM) or 3 dB bandwidth of the measured ring resonators in their critical coupling states are 30.7 pm, 35.8 pm, 35.8 pm, 43.6 pm, corresponding to quality (Q) factors of 50489, 43296, 43296, 35550, respectively. The tap PDs introduce extra loss in the ring cavities, which will limit the Q factor of the rings. The PDs help to monitor the ring status, but they are not strictly necessary if the circuit is fully calibrated and isolated.

The tap PDs couple a fraction of light ($\sim 2\%$) out of the ring and are monitored with an electrical current meter. The monitored photocurrents can help to calibrate the phase shifters (ϕ_1 and ϕ_2). We swept the phase shifters' electrical power in the tunable coupler (ϕ_1) and the ring (ϕ_2). The PD readings are shown in the Supplementary Fig. 18. As shown in the figure, the peak points indicate that the rings are at their critical coupling states, which can hold the highest optical energy. Then the region in-between is the undercoupled state, and the central lowest point is the 0-coupling state, where no light is coupled into the rings. The outer regions are overcoupled states. From these measurements we can also extract that the phase shifter's thermal efficiency is around $28\,\mathrm{mW}/\pi$, then we can use this information to fit all phase delays.

With the locally calibrated phase shifters, we can tune the coupling ratios of all rings to 0 to calibrate the main MZI response, which is shown in Supplementary Fig. 19. When sweeping the phase shifter on one MZI arm, the MZI can reach an extinction ratio of 48.6 dB at 1550 nm at cross state, as shown in Supplementary Fig. 19(b). And the optical spectrum responses with different phase states are shown in Supplementary Fig. 19(c). As can be seen, the highest extinction ratio can only be kept in a small wavelength range due to the dispersion of the used directional couplers.

Based on this calibration data, the whole filter block can now be configured with these phase shifters. First, a Chebyshev type II type bandpass filter is defined, as shown in Supplementary Fig. 20. In this filter configuration, only two rings (R2 and R4) are overcoupled to

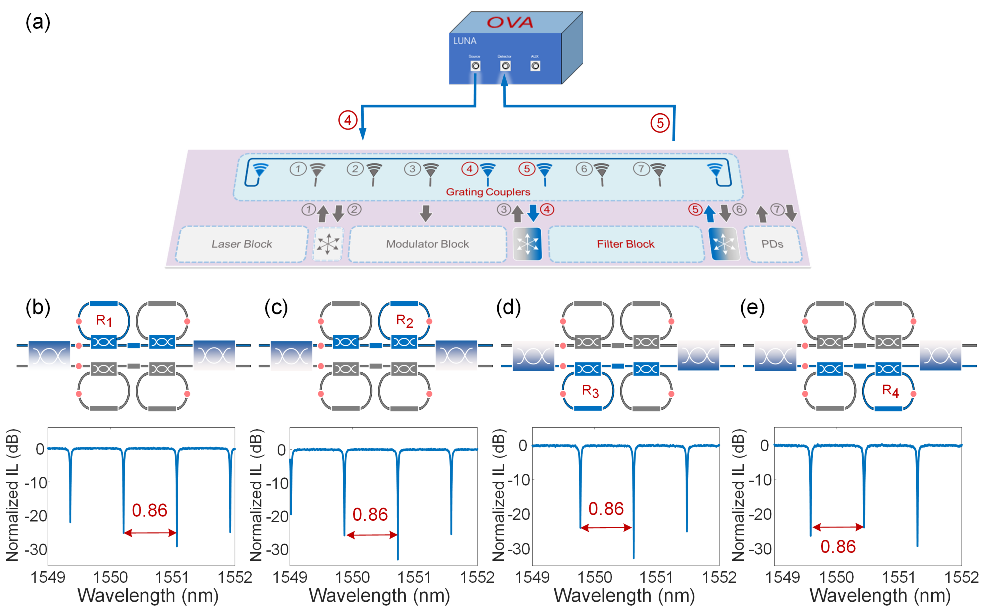

Supplementary Figure 17 (a) The measurement setup for the filter block; (b) Ring 1 measurement configuration and results; (c) Ring 2 measurement configuration and results; (d) Ring 3 measurement configuration and results; (e) Ring 4 measurement configuration and results.

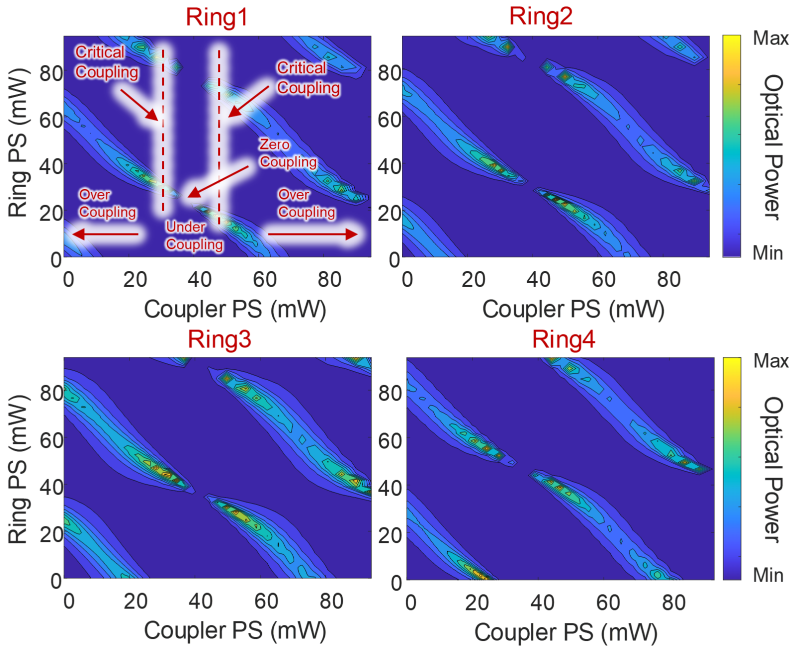

Supplementary Figure 18 Tap monitor reading with the phase shifters tuning. Coupler PS: phase shifter in the tunable coupler (ϕ_1). Ring PS: phase shifter in the ring (ϕ_2).

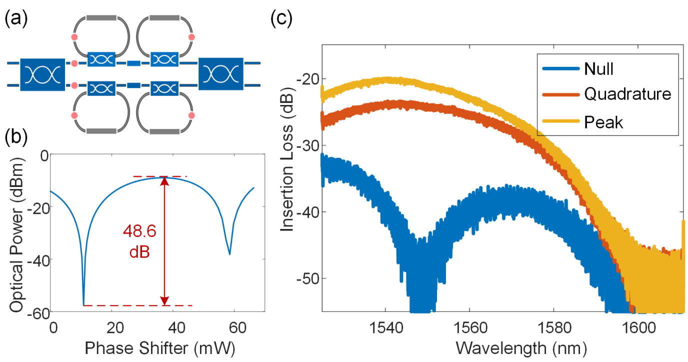

Supplementary Figure 19 (a) The configuration of the MZI measurement. (b) The transmission while sweeping the phase shifter on one arm of the MZI. (c) The spectrum response of the MZI biasing at null point, quadrature point and peak point.

act as all-pass filters, and the other two rings are switched off ($\kappa = 0$), as shown in Supplementary Fig. 20(a). By tuning R2's ring phase, we can get a bandpass filter with a tunable bandwidth, as shown in Supplementary Fig. 20(b). The filter transmission profile shows a passband ripple of 0.5 dB, a roll-off transition of around 210 pm and an extinction ratio of 32 dB. Because of the gradual roll-off, this bandpass filter introduces extra insertion loss when it is too narrow. When the filter bandwidth is narrowed to around 120 pm, the filter introduces 10 dB extra loss. Setting the ring to critical coupling can help to get a sharper roll-off.

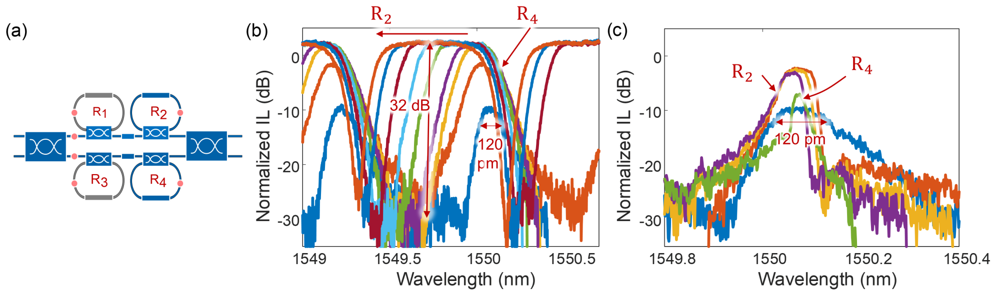

Supplementary Figure 20 (a) The configuration of the filter block for a tunable bandpass filter. (b) A tunable bandpass filter response. Two rings are overcoupled. (c) A tunable bandpass filter response with narrower passbands. Two rings are tuned from overcoupled to undercoupled.

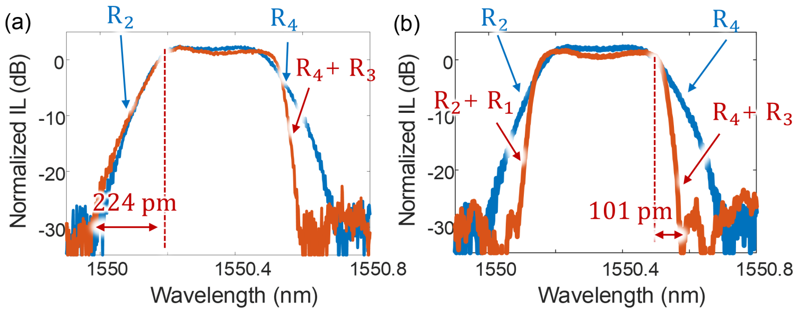

Supplementary Figure 21 (a) R3 is added to improve the roll-off. (b) R1 and R3 are added to improve the roll-off.

As can be seen in Supplementary Fig. 20(c), if R2 is kept over coupled and R4 is tuned to be critically coupled, the bandpass filter can have a narrower (50 pm) bandwidth and a lower loss (3 dB extra loss). And if these two rings are both critically coupled, the filter passband can be as narrow as 29.5 pm with a loss of 7 dB.

The roll-off transition can also be improved with a higher-order filter. As can be seen in Supplementary Fig. 21, extra cascaded ring filters (R1 and R3) can help to increase the all-pass filter order and reach a narrower roll-off transition (from 224 pm to 101 pm). Thus, if higher order filters are required, more ring filters can be added on both arms.

When the ring filters are critically coupled, the ring loss can no longer be neglected and the rings are no longer all-pass filters. If the splitter and combiner's κ of the filter block is set to 0 or 1, the rings act as independent tunable bandstop filters, as shown in Supplementary Fig. 17(b-e). When the splitter and combiner's κ of the filter block is set to 0.5, forming a good MZI, the responses of the MZI with a critically coupled ring are shown in Supplementary Fig. 22. It can be seen that a bandpass filter with a Fano resonance is achieved when the MZI is biased at null point in Supplementary Fig. 22(c). By tuning the ring phase, a tunable bandpass filter is achieved, as shown in Supplementary Fig. 23(a). And if two rings are used, then we can get two pass bands which can be independently tuned, shown in Supplementary Fig. 23(b). The 3 dB bandwidth of these passbands from R1 are around 35 pm, which is slightly larger than the 3 dB bandwidth of R1 (30.7 pm).

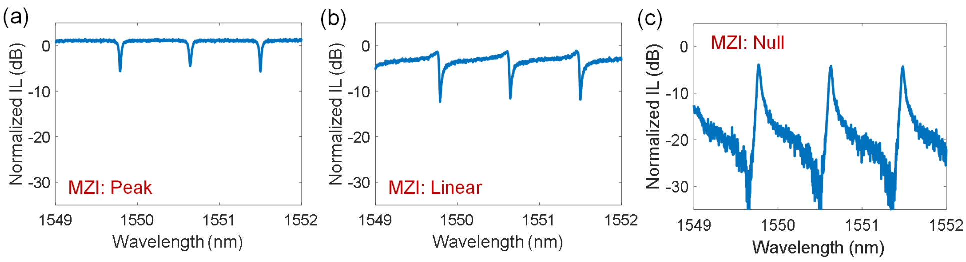

Supplementary Figure 22 Response of a MZI loaded with a critical-coupled ring. (a) MZI biased at peak point; (b) MZI biased at linear point; (c) MZI biased at null point;.

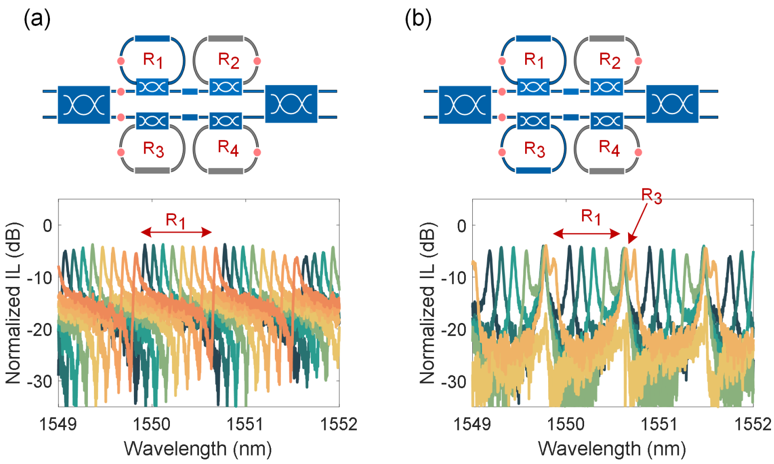

Supplementary Figure 23 (a) A tunable bandpass filter; (b) An independently tunable two pass-band filter.

In conclusion, the filter block of our photonic engine can in principle be configured for arbitrary magnitude responses (limited by the performance of fabricated circuits). We have shown measurement results with bandstop filters (with single rings), bandpass filters (Ring-loaded MZI with critical coupled rings), and flat-top Chebyshev type II type bandpass filters (Ring-loaded MZI with over coupled rings). Thanks to the integrated tap PDs, the system can be monitored and calibrated locally.

3.5 PD Block: High-speed photodiodes

There are two high-speed PDs in our photonic engine for optical-to-electrical conversion. Due to the lack of transimpedance amplifiers (TIA), the PDs are directly wirebonded to the PCB and connected with RF connectors.

The measurement setup and the results are shown in Supplementary Fig. 24. Here, we used an off-chip PD (Discovery Labbuddy DSC10H, 43 GHz, 0.54 A/W at 1550 nm) and an on-chip PD to measure the on-chip modulator's response with the same configuration, and the results are shown in Supplementary Fig. 24(b). Then we can use the off-chip PD's response as a reference to get the on-chip PD's response. The differential result shows a 3 dB bandwidth

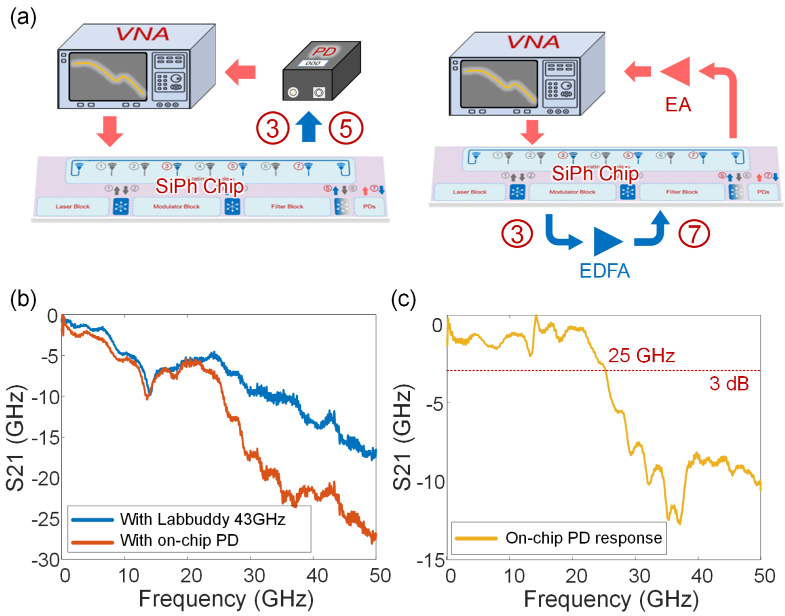

Supplementary Figure 24 (a) RF responses measurement setups with an off-chip PD and with an on-chip PD; (b) The modulator block's RF responses with an off-chip PD and with an on-chip PD; (c) The on-chip PD response using the off-chip PD's response as a reference. VNA: Vector network analyzer. EDFA: Erbium-doped fiber amplifier. EA: Electronic amplifier.

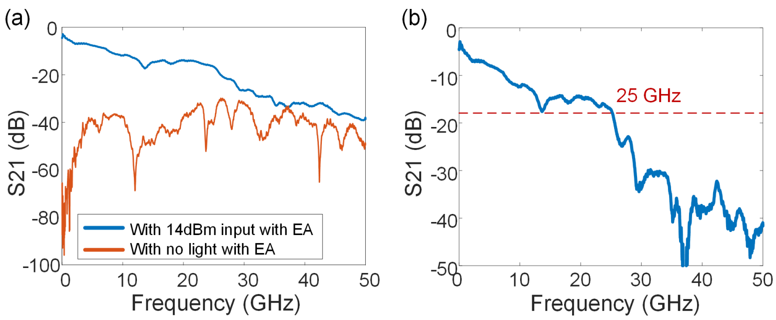

Supplementary Figure 25 (a) A comparison of on-chip PD response and RF crosstalk; (b) The PD response with the crosstalk removed.

of 25 GHz, as shown in Supplementary Fig. 24(c). The PD design is listed as 50 GHz in the PDK document, thus the RF packaging (including the wire-bonding process) limits the PD's bandwidth.

As discussed in Supplementary Section 2, the RF packaging is not ideal and there is a high crosstalk which the RF signal couples from input to output port directly. Comparison of the on-chip PD recovered signal and the electrical crosstalk is shown in Supplementary Fig. 25(a), and the extracted PD response is shown in Supplementary Fig. 25(b). As can be seen, beyond 25 GHz, the PD signal rapidly dropped to the level of the crosstalk . Thus, the packaged system can only work up to 25 GHz. Due to the high crosstalk, the PD recovered signal will be immersed in the crosstalk if only the on-chip laser is used. Thus, we used an off-chip optical amplifier (EDFA) and fed the pumped light back to the on-chip PD. If a better RF packaging and a proper TIA can be implemented, this extra optical amplification is not necessary.

4 Chip Applications

With the characterized and calibrated optical system, we demonstrated several applications with our photonic engine.

4.1 Microwave Photonic Filter

One target application for our photonic engine is microwave photonic filtering between the RF inputs and the RF outputs, using the photonic chip as a black box for the microwave signals. Here we assume an input RF signal $V_{\text{in}}(t)$ as a broadband arbitrary signal. To get the small signal modelling of the system, this input signal can be decomposed as a large offset signal and a small signal variance as:

$$V_{\text{in}}(t) = V_0 + v_{\text{in}}(t) \tag{30}$$

where V_0 is the offset signal and $v_{\text{in}}(t)$ is the small signal. Then the modulated light phase can be expressed as:

$$\begin{aligned}\phi_m &= \frac{\pi}{V_\pi} V_{\text{in}}(t) \\ &= \frac{\pi}{V_\pi}(V_0 + v_{\text{in}}(t))\end{aligned} \tag{31}$$

Instead of using Jacobi-Anger expansion in equation 22 , we can use Taylor expansion around V_0 here to get the linear transfer function of the system:

$$\begin{aligned}e^{-j\phi_m} &= e^{-j\frac{\pi}{V_\pi}V_{\text{in}}(t)} \\ &= (e^{-j\frac{\pi}{V_\pi}V_0} - j\frac{\pi}{V_\pi}e^{-j\frac{\pi}{V_\pi}V_0}v_{\text{in}}(t) - \frac{1}{2}(\frac{\pi}{V_\pi})^2 e^{-j\frac{\pi}{V_\pi}V_0}v_{\text{in}}^2(t) + ...) \\ &= (1 - j\frac{\pi}{V_\pi}v_{\text{in}}(t) - \frac{1}{2}(\frac{\pi}{V_\pi})^2 v_{\text{in}}^2(t) + ...)e^{-j(\frac{\pi}{V_\pi}V_0)}\end{aligned} \tag{32}$$

Take it into equation 21, we can get the output field of the modulator block as:

$$\begin{aligned}E_{\text{out1}} &= [(1-\kappa)\alpha e^{-j\phi_m} - \kappa e^{-j\phi_s}]E_{\text{in1}} \\ &= (1-\kappa)\alpha(1 - j\frac{\pi}{V_\pi}v_{\text{in}}(t) - \frac{1}{2}(\frac{\pi}{V_\pi})^2 v_{\text{in}}^2(t)^2 + ...)e^{-j\frac{\pi}{V_\pi}V_0}e^{-j\omega_c t} \\ &- \kappa e^{-j\phi_s}e^{-j\omega_c t}\end{aligned} \tag{33}$$

for ϕ_s is defined as the phase difference of the two arm, it can cover the static shifts of V_0. If we just focus on the first order of sidelobes, the output field can be simplified as:

$$E_{\text{out1}} \sim [(1-\kappa)\alpha - \kappa e^{-j\phi_s}) + (1-\kappa)\alpha(-j\frac{\pi}{V_\pi}v_{\text{in}}(t)]e^{-j(\omega_c t)} \tag{34}$$

If we assume the modulator phase modulation is linear, the input RF signal $v_{\text{in}}(t)$ can be expressed as a summation of different frequency components, as:

$$\begin{aligned}v_{\text{in}}(t) &= \sum^{\omega_s}(v_s\cos(\omega_s t + \phi_{\omega_s})) \\ &= \sum^{\omega_s}(v_s(\frac{e^{-j(\omega_s t+\phi_{\omega_s})} + e^{j(\omega_s t+\phi_{\omega_s})}}{2}))\end{aligned} \tag{35}$$

Thus the modulated signal can be expressed as:

$$\begin{aligned}E_{\text{out1}} = &\sum^{\omega_s}[(1-\kappa)\alpha - \kappa e^{-j\phi_s})e^{-j\omega_c t} \\ &- j(1-\kappa)\alpha\frac{\pi v_s}{2V_\pi}(e^{-j(\omega_s t+\phi_{\omega_s})} + e^{j(\omega_s t+\phi_{\omega_s})})e^{-j\omega_c t}] \\ &= \sum^{\omega_s}[M_0 e^{-j\phi_{M_0}}e^{-j\omega_c t} + jM_1 v_s(e^{-j(\omega_s t+\phi_{\omega_s})} + e^{-j(-\omega_s t-\phi_{\omega_s})})e^{-j\omega_c t}]\end{aligned} \tag{36}$$

where now

$$\begin{aligned} M_0 e^{-j\phi_{M_0}} &= (1-\kappa)\alpha - \kappa e^{-j\phi_s} \\ M_1 &= -(1-\kappa)\alpha \frac{\pi}{2V_\pi} \end{aligned} \tag{37}$$

By tuning the tunable couplers' coupling ratio κ and the phase shifter ϕ_s in the modulator block, we can arbitrarily set M_0, ϕ_{M_0}, and M_1

For a broadband RF signal modulated light signal, the optical spectrum can be shown as Supplementary Fig. 26(a). If the signal goes through an optical filter, the spectrum will be shaped in magnitude and phase as shown in Supplementary Fig. 26(b). Here we set the transmission of the optical filter as::

- Lower sideband: $L(\omega_c - \omega_s)e^{-j\phi_L(\omega_c-\omega_s)}$
- Upper sideband: $U(\omega_c + \omega_s)e^{-j\phi_U(\omega_c+\omega_s)}$
- Central frequency: $C(\omega_c)e^{-j\phi_C(\omega_c)}$

The filtered optical signal can be expressed as:

$$\begin{aligned} E_{\text{filtered}} = \sum^{\omega_s} [&M_0 C e^{-j(\phi_{M_0}+\phi_c)} e^{-j\omega_c t} + \\ &jM_1 v_s (U e^{-j(\omega_s t + \phi_{\omega_s} + \phi_U)} + L e^{-j(-\omega_s t - \phi_{\omega_s} + \phi_L)}) e^{-j\omega_c t}] \end{aligned} \tag{38}$$

Then the signal is fed into the PD, and the generated photocurrent is:

$$I_{\text{PD}} = \mathcal{R} E_{\text{filtered}} E^*_{\text{filtered}} \tag{39}$$

where $\mathcal{R}$ is the responsivity of the PD. And I_{PD} can be calculated as:

$$\begin{aligned} I_{\text{PD}} = \mathcal{R} \sum^{\omega_s} [&M_0 C e^{-j(\phi_{M_0}+\phi_c)} e^{-j\omega_c t} + \\ &jM_1 v_s (U e^{-j(\omega_s t + \phi_{\omega_s} + \phi_U)} + L e^{-j(-\omega_s t - \phi_{\omega_s} + \phi_L)}) e^{-j\omega_c t}][M_0 C e^{j(\phi_{M_0}+\phi_c)} e^{j\omega_c t} + \\ &jM_1 v_s (U e^{j(\omega_s t + \phi_{\omega_s} + \phi_U)} + L e^{j(-\omega_s t - \phi_{\omega_s} + \phi_L)}) e^{j\omega_c t}] + \text{mixed signal} \\ = &I_{\text{dc}} + I_{1^{st}} + I_{2^{nd}} + \text{mixed signal} \end{aligned} \tag{40}$$

where I_{dc}, $I_{1^{st}}$, $I_{2^{nd}}$ are the DC signal, first order signal (original frequency ω_s), and second order harmonics (doubled frequency $2\omega_s$), respectively. Here again, if we just focus on the

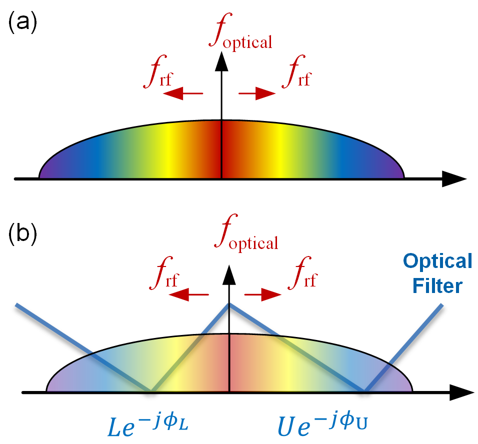

Supplementary Figure 26 (a) Optical spectrum of a modulated light signal; (b) A modulated light signal with an optical filter.

linear response $I_{1^{st}}$ of this microwave photonic filtering system and ignore the mixed signal, we can get that:

$$\begin{aligned} I_{1^{st}} = 2\mathcal{R}\sum^{\omega_s} M_1 M_0 C v_s [U \sin{(\omega_s t + \phi_{\omega_s} + \phi_U - \phi_{M_0} - \phi_C)} \\ + L \sin{(-\omega_s t - \phi_{\omega_s} + \phi_L - \phi_{M_0} - \phi_C)}] \end{aligned} \tag{41}$$

If we get the phase term out, it becomes:

$$\begin{aligned} I_{1^{st}} &= 2\mathcal{R}M_1M_0C[\sum^{\omega_s}(Ue^{-j(\phi_U-\phi_{M_0}-\phi_C-\pi/2)}v_s\cos{(\omega_s t+\phi_{\omega_s})}- \\ &Le^{-j(\phi_L-\phi_{M_0}-\phi_C-\pi/2)}v_s\cos{(\omega_s t+\phi_{\omega_s})})] \\ &= 2\mathcal{R}M_1M_0C[Ue^{-j(\phi_U-\phi_{M_0}-\phi_C-\pi/2)} - Le^{-j(\phi_L-\phi_{M_0}-\phi_C-\pi/2)}]v_{\text{in}}(t) \end{aligned} \tag{42}$$

This shows the full expression of the linear frequency response, and it can be rewritten as:

$$I_{1^{st}} = |H_{\omega_s}|e^{-j\phi_{\omega_s}}v_{\text{in}} \tag{43}$$

where

$$\begin{aligned} |H_{\omega_s}| &= |2\mathcal{R}M_1M_0C\sqrt{U^2+L^2-2UL\cos{(\phi_U+\phi_L-2(\phi_{M_0}+\phi_C))}}| \\ \phi_{\omega_s} &= \arctan(\frac{-U\cos{(\phi_U-(\phi_{M_0}+\phi_c))}+L\cos(\phi_L-(\phi_{M_0}+\phi_c))}{U\sin{(\phi_U-(\phi_{M_0}+\phi_c))}+L\sin(\phi_L-(\phi_{M_0}+\phi_c))}) \end{aligned} \tag{44}$$

and in which

$$\begin{aligned} M_0e^{-j\phi_{M_0}} &= (1-\kappa)\alpha - \kappa e^{-j\phi_s} \\ M_1 &= -(1-\kappa)\alpha\frac{\pi}{2V_\pi} \end{aligned} \tag{45}$$

Thus, we got the full transfer function for the original frequency ω_s :

$$\begin{aligned} H &= 2\mathcal{R}M_1M_0C[Ue^{-j(\phi_U-\phi_{M_0}-\phi_C-\pi/2)} - Le^{-j(\phi_L-\phi_{M_0}-\phi_C-\pi/2)}] \\ &= |H_{\omega_s}|e^{-j\phi_{\omega_s}} \end{aligned} \tag{46}$$

In reality, the used phase modulator cannot have a perfect linear phase response, while the tuning of modulator's κ and ϕ_s can help to linearize the phase modulation [8], and the tuning of the optical filter (U and L) can compensate the imperfection. Thus, this system works with slightly tuned parameters when an imperfect phase modulator is used.

If we make an assumption that the lower sideband region of the optical transmission spectrum (L) and the upper sideband region (U) are fully independent (which is not true for continuous broadband spectrum transmissions, but is a valid assumption for microwave signals modulated on a carrier frequency), the microwave photonic filter design can also use allpass filters to define a filter function similar to the optical filter design discussed in Supplementary Section 3.4. The "splitter" and "combiner" in this "interferometer" are implemented by the modulator and PD, which can be regarded as perfect 50:50 coupling ratio without any insertion loss, and the all-pass filter can still be ring resonators, and then it can also be regarded as a difference of two all-pass filters, as shown in equation 46. Because the ring resonators will both work in the upper and lower sidebands, the design method can only be used for half of the FSR of the ring resonators (in our case, 53.5 GHz), and in the other half the spectral response will be the image of the first one.

Here we show some demonstrations for the RF filter design. If the reconfigurable modulator is set as a phase modulator and the filter block is set as a single notch filter (a critical coupled ring resonator), we can achieve a single bandpass filter in the RF domain, as shown in Supplementary Fig. 27(a). If two rings are used, a double bandpass filter or one-pass one-stop band filter can be realized, where the difference is that the second ring is under/critically coupled (shown in Supplementary Fig. 3(b)), or overcoupled (shown in Supplementary

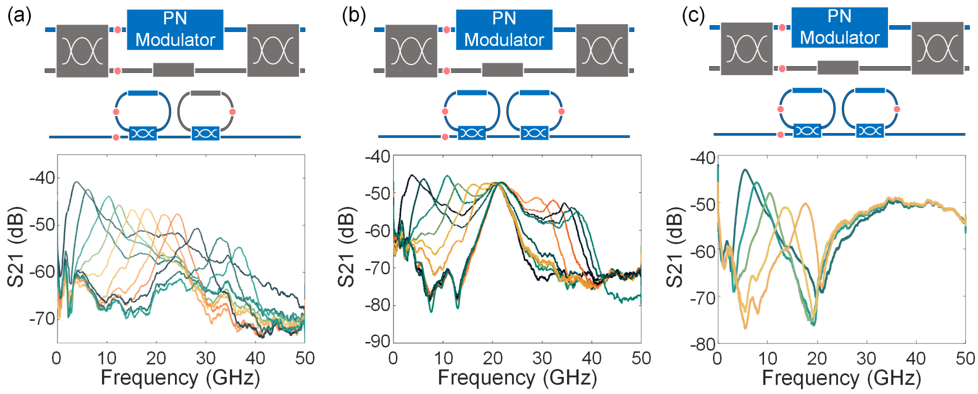

Supplementary Figure 27 (a) Microwave filter: single tunable bandpass filter; (b) Microwave filter: double tunable bandpass filter; (c) Microwave filter: tunable one-pass one-stop band filter.

Fig. 3(c)). This modulator configuration is set for the $\kappa = 0$, thus $\phi_{A_0} = 0$ in equation 24, and these RF filtering results fully match the optical filtering response when single ring or double rings used in an MZI biasing at null point (Supplementary Fig. 23).

If the ring resonators are overcoupled, they act as all-pass filters for the RF signal loaded onto the light carrier. By tuning the modulator block and the cascaded rings (R1 and R2), we can get tunable low-pass filters (LPF), high-pass filters (HPF), and bandpass filters (BPF), as shown in Supplementary Fig. 28. Supplementary Fig. 28(a), (d), and (h) show the measured S21 responses of the tunable filters, but these responses are enveloped by the response of the original modulator and PD response. Thus we constructed an "all pass" reference which combines the widest HPF and the widest LPF, as shown in Supplementary Fig. 28(g), and all other curves are calibrated with the reference curve, which are shown in Supplementary Fig. 28(b) and (e). These responses more clearly show the high-pass and low-pass behaviors. The curves are further normalized by removing the insertion loss in Supplementary Fig. 28(c) and (f). Because the responses below -70 dB are close to the noise floor at high frequency, the low-pass filter responses are not accurate at the high frequency points, thus we truncate the responses in Supplementary Fig. 28(c) to 30 GHz, to make it more clear. Supplementary Fig. 28(h) shows a tunable BPF response. Because of the large roll-off of the optical ring resonator, these band-pass filters show higher losses than previous filters. The normalized BPF responses are shown in Supplementary Fig. 28(i). The high-pass, low-pass and band-pass filters are realized with the same mechanism as the optical band-pass filters discussed in Supplementary Fig. 20, while the RF filters are in a narrower frequency/wavelength range (30 GHz to 240 pm range at 1550 nm).

The full optical filter block can also be used to form microwave photonic filters. The final RF responses can be fully predicted with equation 34, but its filter synthesis will be hard. Supplementary Fig. 29 shows a four pass-band filter where these four bands can be independently tuned and suppressed.

One important application of the microwave photonic filter is an RF equalizer. Here we implement it for our intensity modulator with PDs. The results can be seen in Supplementary Fig. 30. The curves in Supplementary Fig. 30 are the raw data from VNA and not calibrated with other data, which means that all cables, bonding wires and other components' response are included. It shows that the microwave filter based equalizer can flatten the response of

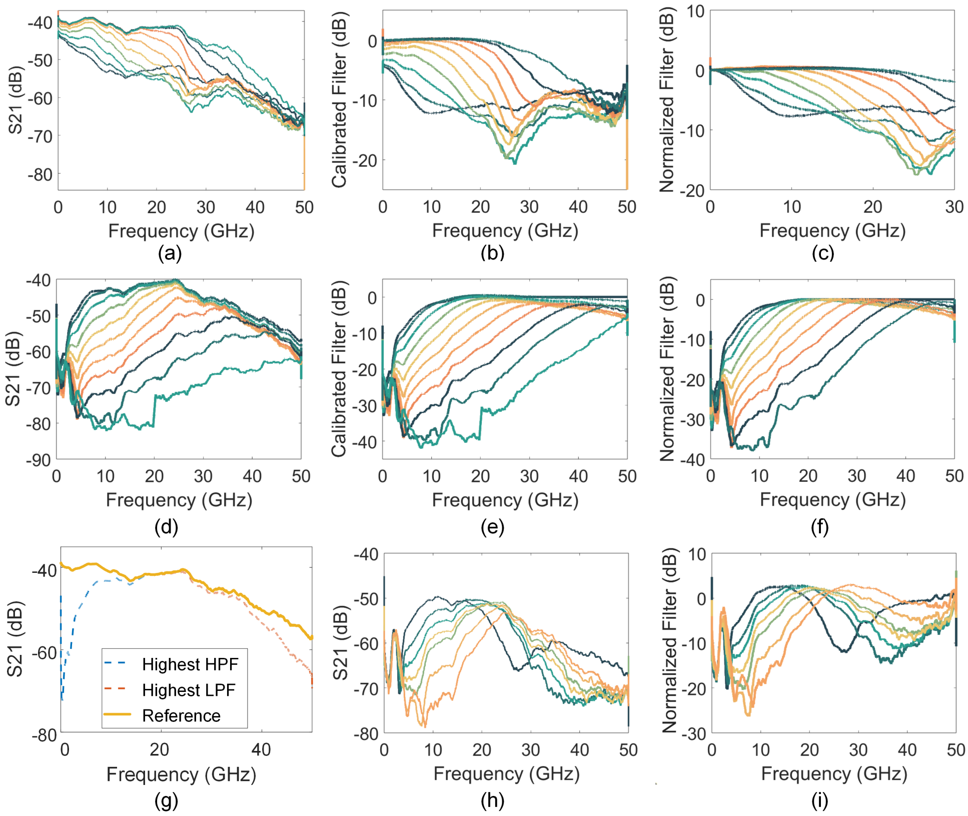

Supplementary Figure 28 (a) Measured S21 response of a tunable low-pass filter (LPF); (b) Using the highest one as a reference, calibrated filter response of the tunable LFP; (c) Normalized filter response of the tunable LFP; (d) Measured S21 response of a tunable high-pass filter (HPF); (e) Using the highest one as a reference, calibrated filter response of the tunable HPF; (f) Normalized filter response of the tunable HPF; (g)A "all pass" reference curve generated from the highest HPF and highest LFP, to calibrate the remaining filters. (h) Measured S21 response of a tunable band-pass filter (BPF); (i) Normalized filter response of the tunable BPF.

the whole system with an off-chip PD up to 26 GHz (Supplementary Fig. 30(a)) and with an on-chip PD up to 25 GHz (Supplementary Fig. 30(b)).

The proposed photonic engine has been demonstrated several microwave photonic functionalities. In this section, we evaluate its basic figures of merit (FOM), including RF link gain, noise figure and spurious-free dynamic range (SFDR). Because we lack proper TIAs, the on-chip PDs suffer from high losses, and the link gain will be very low, and therefore the noise figure will be very high. We evaluate the link with an off-chip PD for meaningful results.

In addition, we evaluated the figure of merits of the microwave photonic link using our photonic engine.

RF Gain The measurement of the RF gain for this system occurs with the modulator configured as an intensity modulator. Referencing 13, with a PD current of 3.2 mA and the modulator in intensity mode, the total link gain registers approximately −35 dB. This

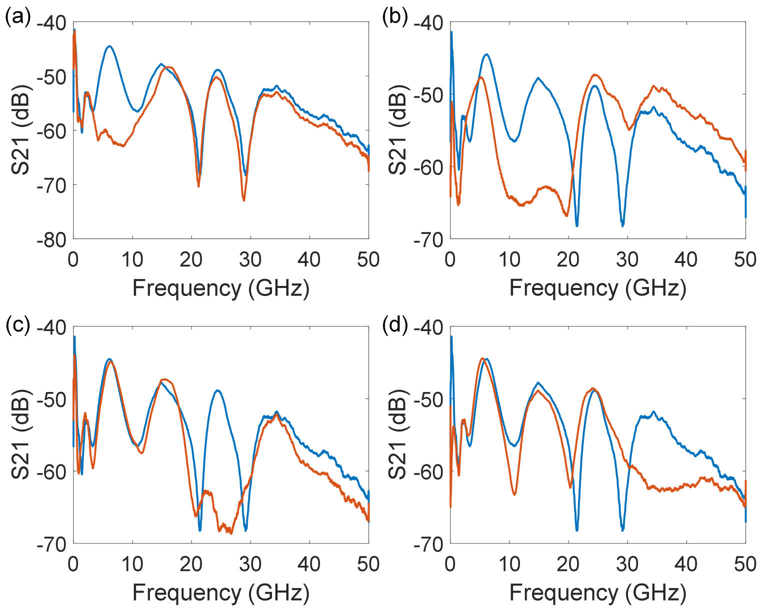

Supplementary Figure 29 A tunable four band-pass filter and its first (a), second (b), third(c), and forth(d) pass-band suppressed filter.

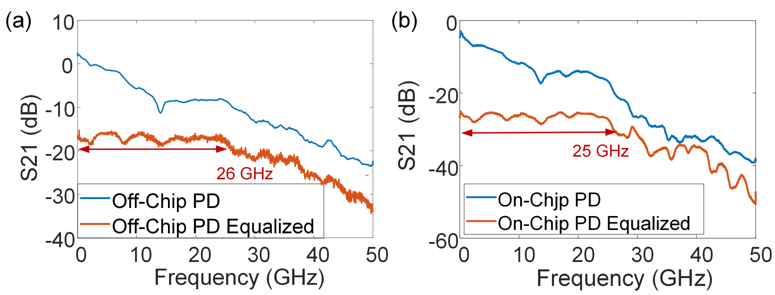

Supplementary Figure 30 (a) Equalized transmission spectrum with an off-chip PD; (b) Equalized transmission spectrum with an on-chip PD

significant RF loss stems from the low modulation depth of the PN junction and the low responsivity of the off-chip PD, optimized for high bandwidth.

If the modulator is tuned to a phase modulator configuration, the link gain would be suppressed as low as -60 dB, which means that the entire RF link can work as a tunable RF attenuator.

Noise Figure The noise figure is determined by the RF gain, and the increase of the noise floor. In order to measure the noise floor of the system, we cascaded three amplifiers, which provide 48 dB amplification in total, to pump up the noise levels, as shown in Supplementary Fig. 31. The spectrum analyzer (Keysight N9010A) has a noise floor of -124 dBm at bandwidth of 2 Hz. With the connected amplifiers, the thermal noise at room temperature

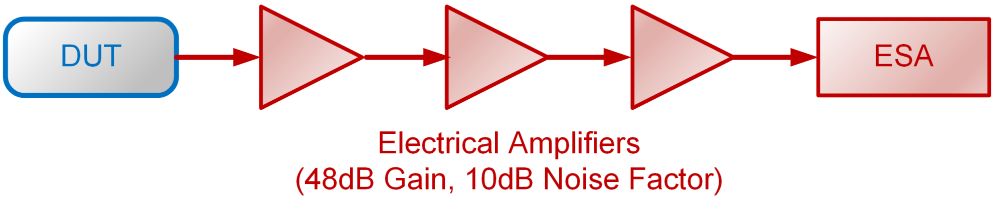

Supplementary Figure 31 Setup for the noise floor measurements. DUT: Device under test; ESA: Electrical spectrum analyzer.

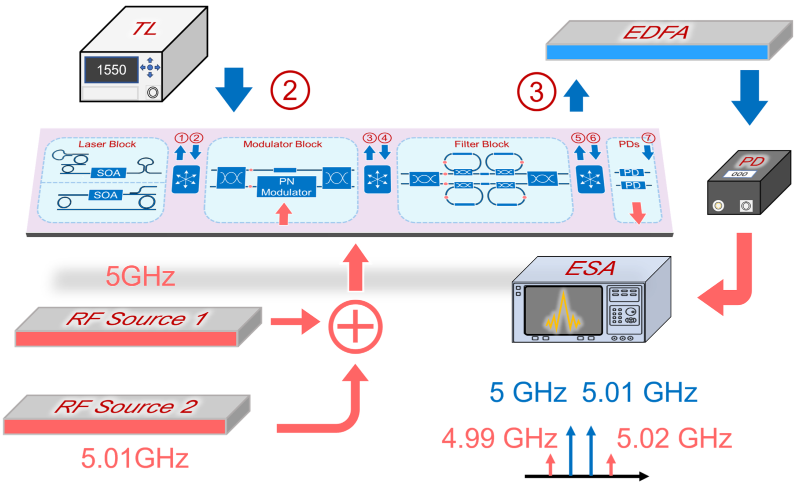

Supplementary Figure 32 Setup for the SFDR measurement.

($-174\,$dBm/Hz) is measured around $-111\,$dBm (a $50\,\Omega$ resistor is connected to the amplifiers as input). If the amplifiers inputs are connected to the output of the off-chip PD with a photocurrent of $5\,$mA (On-chip laser output $-3\,$dBm, amplifed by an EDFA), the noise floor will raise up to $-92.5\,$dBm, indicating a $18.5\,$dB of noise power increase. Thus, the noise figure of this photonic engine is around $53.5\,$dB. To intrinsically improve the NF, we can add extra SOA with higher saturation power to boost the laser power in our system. While, higher optical may introduce nonlinearities in the used silicon waveguides, like two photon absorption. However, higher optical power may introduce nonlinearities in the silicon waveguides, such as two-photon absorption. Using wider silicon waveguides or SiN waveguides (now available in some silicon photonic platforms) can help mitigate the optical power limitations. Alternatively, we can employ a longer modulator or a dual-drive modulator to achieve higher modulation efficiency.

SFDR We also characterize the SFDR of this photonic engine. The measurement setup is shown in Supplementary Fig. 32. As can be seen, two RF sources are used to generate a two-tone signal (5 GHz and 5.01 GHz). This two-tone signal is modulated on an optical carrier, which is generated by an off-chip tunable laser source (to reduce the crosstalk from onchip laser). The modulated signal is guided off-chip, amplifed by an EDFA, and then received by a PD. Because of the nonlinear response of the modulator and the PD, the generated RF signal will contain intermodulation distortion, characterized by the IM3 products, which in this case

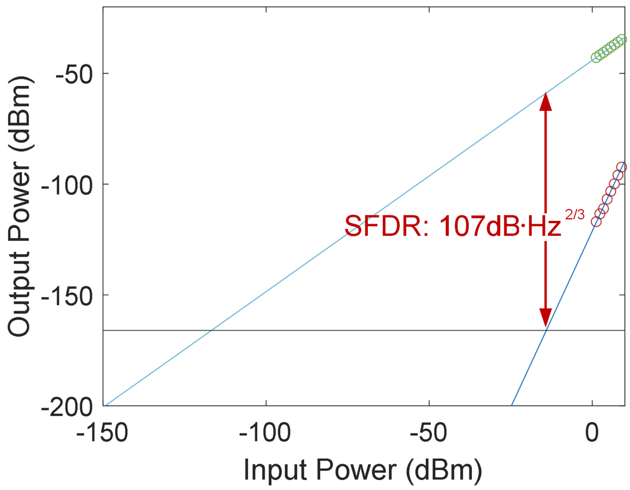

Supplementary Figure 33 Measured SFDR of this microwave processor.

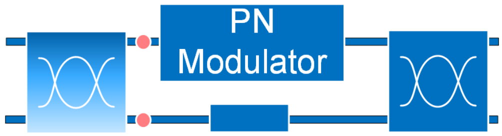

Supplementary Figure 34 Modulator block configuration for frequency doubling, where more light is guided to the PN modulator for compensating its insertion loss.

are 4.99 GHz and 5.02 GHz. By sweeping the input signal power from the RF sources, and recording the power of the generated fundamental and IM3 signal, we can get the SFDR of this RF transmission system as 107 $\mathrm{dBHz}^{2/3}$ for a noise floor of -164.5 dBm/Hz [12]. The result is shown in Fig 33.

In the future work, we can integrate proper TIAs with our on-chip PDs, then the performance of the entire system could be measured and evaluated.

4.2 Frequency Multiplier

Another application for our photonic engine is the frequency multiplier. Here we used the modulator block to achieve frequency doubling with high original signal extinction. It is based on the carrier-suppressed double-sideband modulation scheme with the reconfigurable modulator, the configuration of which is shown in Supplementary Fig. 34 [13]. The main advantage of the system is that the tunable splitter used in the modulator block can be tuned to compensate the extra loss of the used modulator, and then reach a very high carrier extinction.

Demonstrations were implemented with our photonic engine, as shown in Supplementary Fig. 35. Here we used an RF source (R&S SMA40) as an RF signal generator. The generated RF signal will be modulated on the laser carrier (from the on-chip laser block) by the modulator block, and then the modulated light signal will be coupled to a PD. The recovered RF

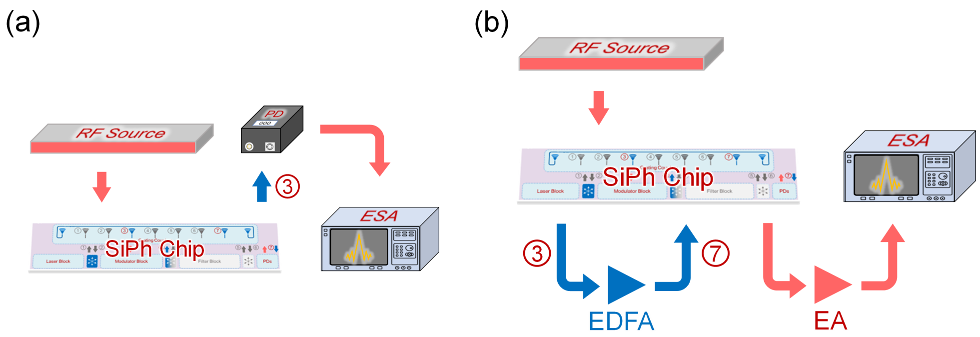

Supplementary Figure 35 (a) A demonstrator for frequency doubling with an off-chip PD; (b) A demonstrator for frequency doubling with an on-chip PD. SiPh Chip: Silicon photonic chip. EDFA: Erbium-doped fiber amplifier. EA: Electronic amplifier. ESA: Electrical spectrum analyzer.

signal was fed into a spectrum analyzer. The frequency-doubling results are shown in Supplementary Fig. 36. In this part, the extinction ratio is calculated by the second harmonic signal power to the original frequency signal power. As can be seen, normal intensity modulation can keep the second harmonic signal 40 dB below the original frequency, while if the modulator is biased at null point, the second harmonic signal can be 40 dB higher than the original one. The extinction ratio's drop is mainly due to the system RF loss for higher frequency.

We also did the same measurement with an on-chip PD (Supplementary Fig. 35(b)), and the results are shown in Supplementary Fig. 37. As it is shown, this frequency doubling can also work for 20 GHz, but the extinction ratio degenerates a lot at the higher frequencies. This is due to the high RF crosstalk at high frequencies, where the first-order signal is not from the optical signal but is from the direct coupling crosstalk, which can be seen in Supplementary Fig. 37(b). One thing that should be noted is that the first-order signal power is lower than the crosstalk below 10 GHz, which may because of the RF signal destructive interference between the light generated RF signal with the crosstalk RF signal.

4.3 Opto-electronic Oscillator

Our photonic engine can not only generate optical signals with the on-chip laser block, but also can form the heart of an opto-electronic oscillator for RF signal generation, when we combine the chip with external amplifiers and a fiber delay line. Here, too, we performed the tests both with an off-chip PD or an on-chip PD, and their schematics are shown in Supplementary Fig. 38. Here, the on-chip laser, modulator, optical filter blocks, as well as PDs formed a tunable bandpass microwave photonic filter, as shown in Supplementary Fig. 27(a). The modulated RF signal is loaded on the optical link, filtered, amplified by an electronic amplifier and then fed back into the modulator as an RF source. The whole system thus becomes an RF loop, and it will start oscillating if the net gain is 0 dB or higher. By tuning the pass-bands of the microwave photonic filter, as discussed in the Supplementary Section 4.1, we can tune the oscillation RF frequency and achieve a tunable RF source. A length of extra fiber was added to the system, which extends the entire cavity to achieve a lower RF phase noise.

The RF generation results with the off-chip PD are shown in Supplementary Fig. 39. Here, the extra fiber added is 500 m long. The spectrum of generated RF signals is shown in

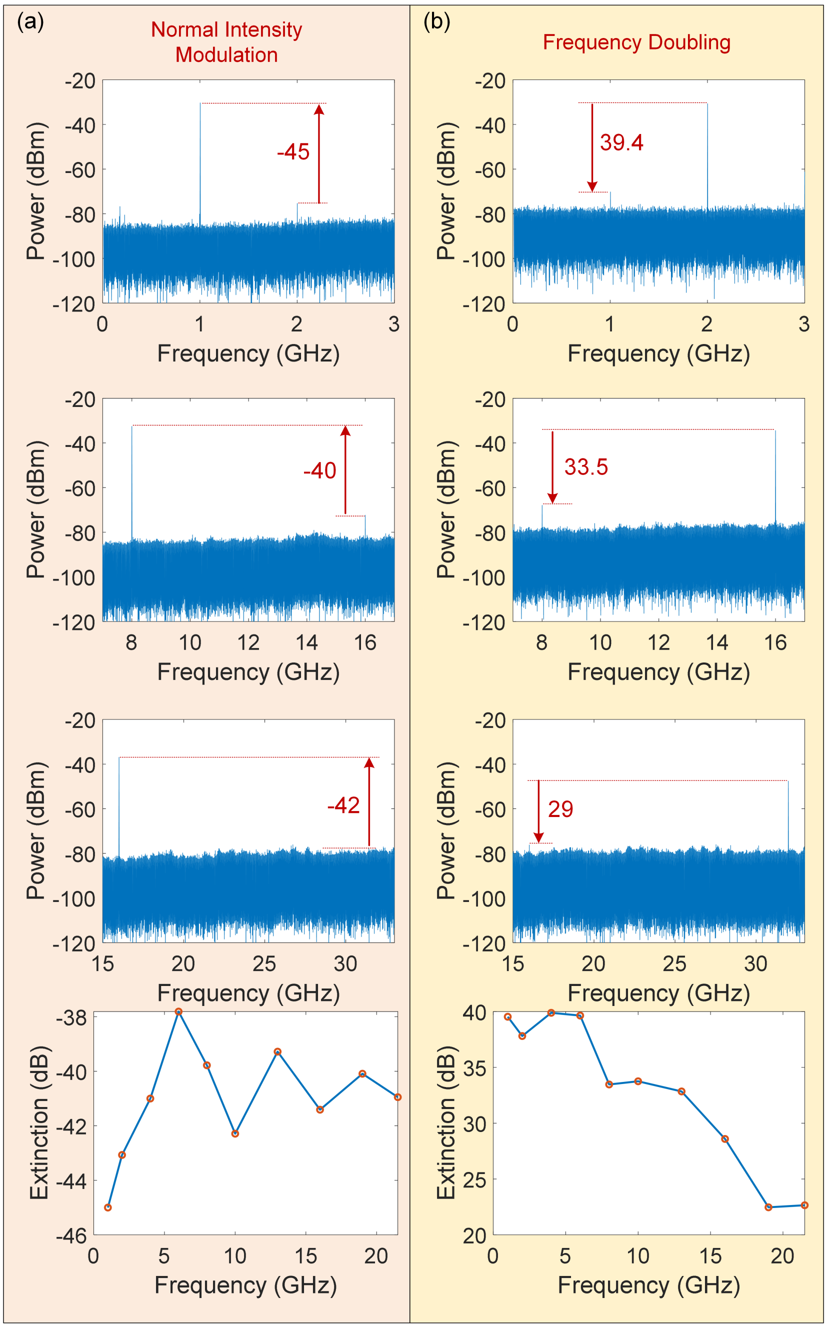

Supplementary Figure 36 Frequency multiplying results with an off-chip PD. (a) Normal intensity modulation when the modulator MZI is biased at quadrature point; (b) Frequency doubling when the modulator MZI is biased at null point.

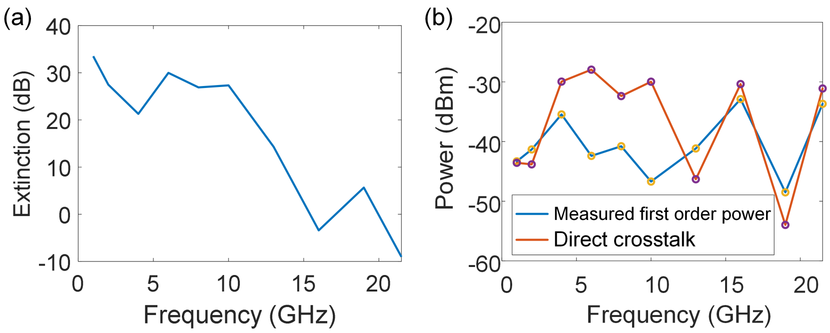

Supplementary Figure 37 Frequency multiplying results with an on-chip PD. (a) Frequency doubling when the modulator MZI is biased at null point. (c) Measured first order signal power and directly coupled crosstalk power.

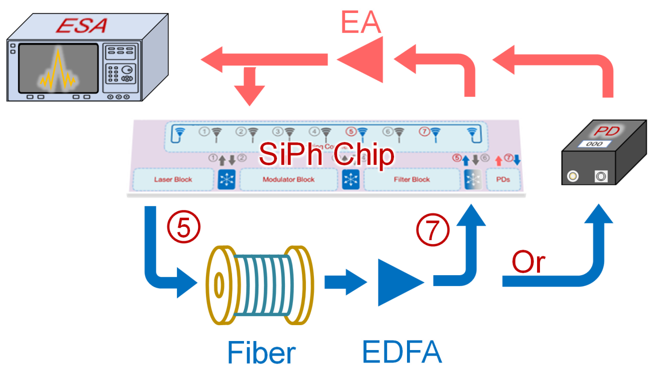

Supplementary Figure 38 An opto-electronic oscillator demonstrator incorporating the single chip photonic engine. SiPh Chip: Silicon photonic chip. EDFA: Erbium-doped fiber amplifier. EA: Electronic amplifier. ESA: Electrical spectrum analyzer.

Supplementary Fig. 39(a) and (b). As can be seen, the signal frequency can be tuned from 3.8 GHz to 24.1 GHz, and higher frequencies can be reachable, but limited by the used ESA (Anritsu MS2840A, 26 GHz). The zoom-in spectrum shows that the mode spacing of this oscillator is around 400 kHz and the sidelobe extinction is 32 dB. Supplementary Fig. 39(c) and (d) show the phase noise of the generated signal. It can be noted that the strength of the phase noise is almost constant for all the generated signals.

Demonstrators with on-chip PDs are also implemented, and the results are shown in Supplementary Fig. 40. Here, the extra fiber added is 20 m long, and the oscillator cannot keep a single mode oscillation with a longer fiber. The spectrum of the generated RF signals are shown in Supplementary Fig. 40(a) and (b). As can be seen, the signal frequency can be tuned from 3.3 GHz to 11.6 GHz. The zoom-in spectrum shows that the mode spacing of this oscillator is around 4 MHz and the sidelobe extinction is 18.7 dB. Supplementary Fig. 39(c) and (d) show the phase noise of the generated signal. From this we can see that with the on-chip PD, the oscillator has a higher noise than with an off-chip PD (−97 dBc/Hz at 100 kHz

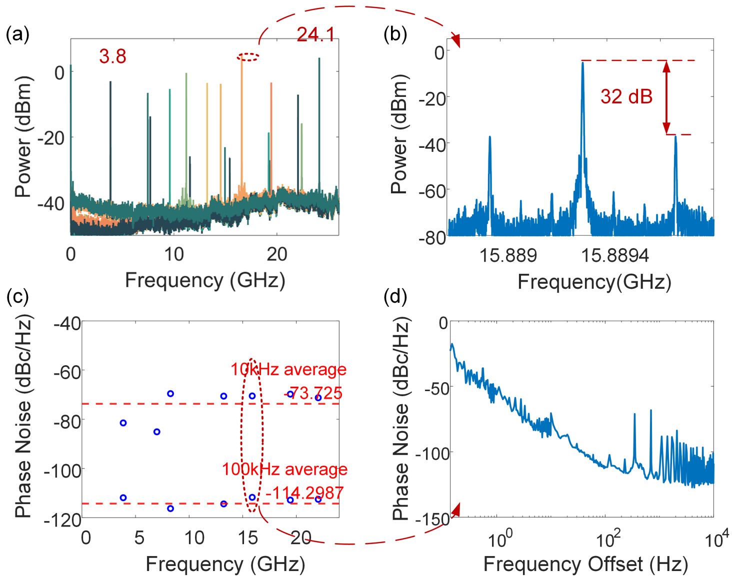

Supplementary Figure 39 (a) Tunable RF signal generation from 3.8 GHz to 24.1 GHz with an off-chip PD; (b) The zoom-in spectrum of generated 15.8 GHz signal; (c) Extracted phase noises of the generated RF signals; (d) Phase noise results of the generated 15.8 GHz signal.

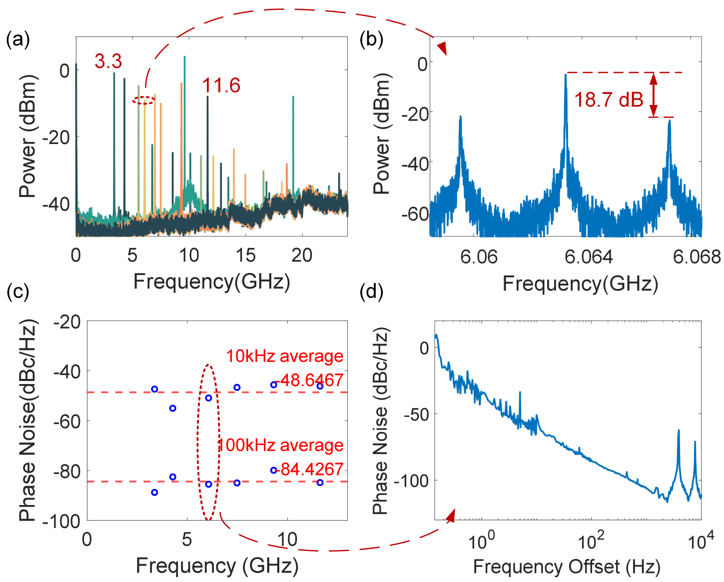

Supplementary Figure 40 (a) Tunable RF signal generation from 3.3 GHz to 11.6 GHz with an on-chip PD; (b) The zoom-in spectrum of generated 6.06 GHz signal; (c) Extracted phase noises of the generated RF signals; (d) Phase noise results of the generated 6.06 GHz signal.

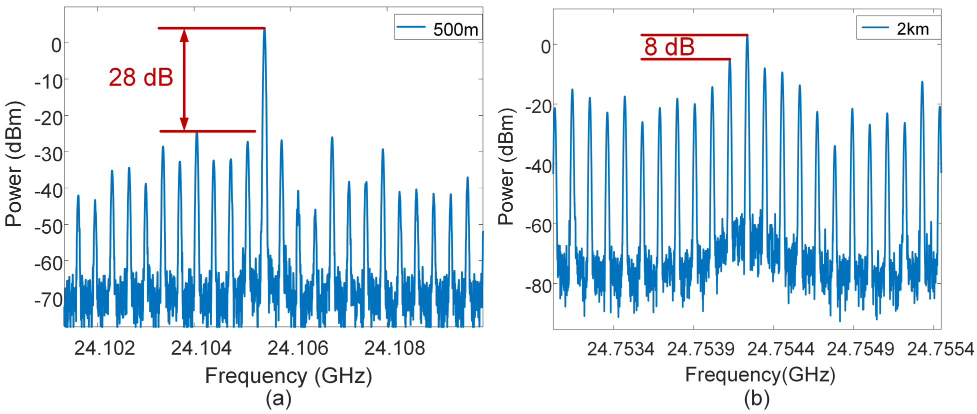

Supplementary Figure 41 (a) RF signal spectrum generated with an off-chip PD and 500 mfiber; (b) RF signal spectrum generated with an off-chip PD and 2000 mfiber;

offset with 20 m fiber), which is due to the RF packaging crosstalk. And crosstalk also makes the oscillator unstable to operate beyond 11.6 GHz.

Longer fiber links can help reduce the phase noise of the generated signal. We tested our system using a 2 km fiber in conjunction with the off-chip PD and found that the system could not maintain single-mode oscillation. The results are shown in Supplementary Fig. 41. It can be seen that the sidelobe extinction ratio is only 8 dB with the 2 km fiber link.

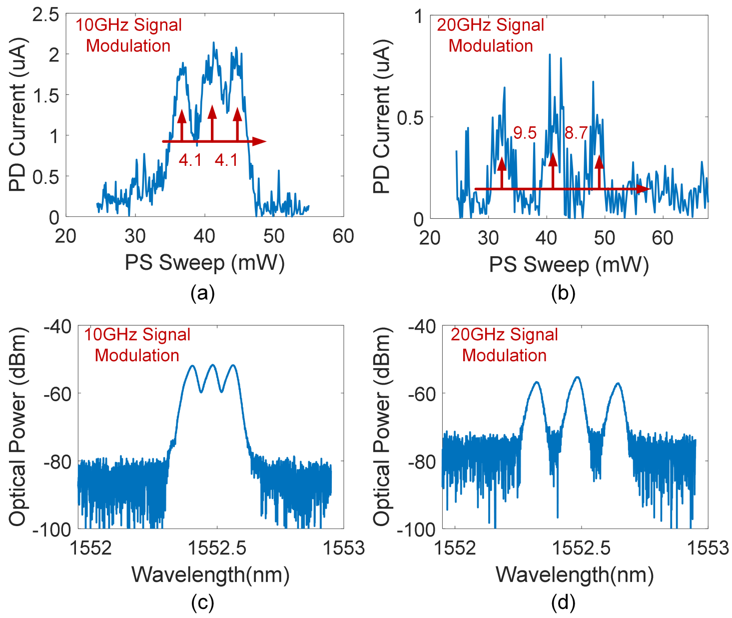

Supplementary Figure 42 A demonstrator as an optical wavelength meter or an RF frequency meter. (a) and (c) The light carrier with 10 GHz RF signal modulated sidelobes; (b) and (d) The light carrier with 20 GHz RF signal modulated sidelobes. (a) and (b) is measured with current meter from tap PD's photocurrent. (c) and (d) is measured with an optical spectrum analyzer.

4.4 Other applications

Apart from the applications discussed above, our photonic engine has more possibilities. Here we show that it can work as an optical wavelength meter or RF frequency meter.

The optical wavelength meter or the RF frequency meter is based on the ring resonators in the filter block. The optical power in the ring can be read with the tap PD. Then if we sweep the phase shifter in the ring, we can know the power distribution along the wavelength or frequency within one FSR of the ring. The results are shown in Supplementary Fig. 42. To avoid that the main lobe fully covers the sidelobes, the modulator block is configured to have a carrier-suppressed (not fully) modulation. From Supplementary Fig. 42 (a) and (b) we can see that the optical carriers and modulation introduced sidelobes can be easily recognized from the PD's readout. Compared with the measurement results from an optical spectrum analyzer Supplementary Fig. 42 (c) and (d), the overall shape are revealed in Supplementary Fig. 42 (a) and (b). The frequency measured (a) 7.8 GHz and (b) 17.1 GHz are not accurate, but a more dedicated calibration could overcome this limitation. The spectral resolution of this optical wavelength meter or RF frequency meter is determined by the 3 dB bandwidth of the used ring resonator. A ring resonator with a higher Q factor can therefore reach a higher spectral resolution.

5 Conclusion

In conclusion, the single-chip photonic engine presented in this study serves as a versatile reconfigurable filter for both optical signals (3.4) and RF signals (4.1), while also providing optimized electro-optical (E/O) (3.3) and opto-electrical (O/E) conversions (3.5). The implementation of tunable laser sources through micro-transfer-printing allows for an impressive tuning range of up to 90 nm (3.1). The system's flexibility is enhanced by using multiple monitor detectors, enabling local configuration. Furthermore, the processor exhibits remarkable capabilities in RF signal generation (4.3) and RF frequency doubling (4.2). Overall, this demonstration offers a promising and comprehensive approach to generating, distributing, and processing both optical and RF signals, with potential applications in data centers, wireless and satellite communication, and various optical and microwave fields. The seamless integration of functionalities on a single chip represents a significant advancement in signal processing technology.

References

[1] Ferraro, F. et al. Imec silicon photonics platforms: performance overview and roadmap. https://doi.org/10.1117/12.2650579 **12429**, 22–28 (2023).

[2] Pantouvaki, M. et al. Active Components for 50 Gb/s NRZ-OOK Optical Interconnects in a Silicon Photonics Platform. Journal of Lightwave Technology **35**, 631–638 (2017).

[3] Zhang, J. et al. Micro-transfer printing InP C-band SOAs on advanced silicon photonics platform for lossless MZI switch fabrics and high-speed integrated transmitters. Optics Express, Vol. 31, Issue 26, pp. 42807-42821 **31**, 42807–42821 (2023). URL https://opg.optica.org/viewmedia.cfm?uri=oe-31-26-42807&seq=0&html=truehttps://opg.optica.org/abstract.cfm?uri=oe-31-26-42807https://opg.optica.org/oe/abstract.cfm?uri=oe-31-26-42807.

[4] Tran, M. A., Huang, D. & Bowers, J. E. Tutorial on narrow linewidth tunable semiconductor lasers using Si/III-V heterogeneous integration. APL Photonics **4**, 111101 (2019). URL /aip/app/article/4/11/111101/1061823/Tutorial-on-narrow-linewidth-tunable-semiconductor.

[5] Roelkens, G. et al. Present and future of micro-transfer printing for heterogeneous photonic integrated circuits. APL Photonics **9**, 10901 (2024). URL /aip/app/article/9/1/010901/2932278/Present-and-future-of-micro-transfer-printing-for.

[6] Wang, M., Ribero, A., Xing, Y. & Bogaerts, W. Tolerant, broadband tunable 2 $\times$ 2 coupler circuit. Optics Express **28**, 5555 (2020).

[7] Miller, D. A. B. Perfect optics with imperfect components. Optica, Vol. 2, Issue 8, pp. 747-750 **2**, 747–750 (2015). URL https://opg.optica.org/viewmedia.cfm?uri=optica-2-8-747&seq=0&html=truehttps://opg.optica.org/abstract.cfm?uri=optica-2-8-747https://opg.optica.org/optica/abstract.cfm?uri=optica-2-8-747.

[8] Deng, H. & Bogaerts, W. Pure phase modulation based on a silicon plasma dispersion modulator. Optics Express **27**, 27191 (2019).

[9] Willson, A. N. & Orchard, H. J. Insights into Digital Filters Made as the Sum of Two Allpass Functions. IEEE Transactions on Circuits and Systems I: Fundamental Theory and Applications **42**, 129–137 (1995).

[10] Madsen, C. K. & Zhao, J. H. Optical Filter Design and Analysis. Optical Filter Design and Analysis (1999).

[11] Bogaerts, W. et al. Silicon microring resonators. Laser & Photonics Reviews **6**, 47–73 (2012). URL http://doi.wiley.com/10.1002/lpor.201100017.

[12] Daulay, O. et al. Ultrahigh dynamic range and low noise figure programmable integrated microwave photonic filter. Nature Communications 2022 13:1 **13**, 1–8 (2022). URL https://www.nature.com/articles/s41467-022-35485-x.

[13] Deng, H. & Bogaerts, W. Configurable Modulator based Optical Carrier Frequency Suppressed Intensity Modulation. 2022 IEEE Photonics Society Summer Topicals Meeting Series, SUM 2022 - Proceedings (2022).